2014

Validation Study Of The Integral-Differential Scheme For Multi-Block Grids

Honest Frank Mrema

North Carolina Agricultural and Technical State University

Validation Study of the Integral-Differential Scheme for Multi-Block Grids

Honest Frank Mrema

North Carolina A&T State University

A thesis submitted to the graduate faculty

in partial fulfillment of the requirements for the degree of

MASTER OF SCIENCE

Department: Mechanical Engineering

Major: Mechanical Engineering

Major Professor: Dr. Frederick Ferguson

Greensboro, North Carolina

2014

The Graduate School
North Carolina Agricultural and Technical State University
This is to certify that the Master's Thesis of

Honest Frank Mrema

has met the thesis requirements of
North Carolina Agricultural and Technical State University

Greensboro, North Carolina
2014

Approved by:

Dr. Frederick Ferguson Major Professor	Dr. John Kizito Committee Member
Dr. Arturo Fernandez Committee Member	Dr. Mookesh Dhanasar Committee Member
Dr. Samuel Owusu-Ofori Department Chair	Dr. Sanjiv Sarin Dean, The Graduate School

Biographical Sketch

Honest Frank Mrema was born on May 11, 1989 in Tanzania. He received his Bachelor of Science degree in Aerospace Engineering from the University of Tennessee in 2012. He is a candidate for the Master of Science degree in Mechanical Engineering at North Carolina Agricultural and Technical State University.

Dedication

I dedicate this thesis to my parents, siblings, and loving wife Tasha Mrema

Acknowledgements

Without the grace of God, I would not have accomplished this task. For that reason, all honor and glory goes to God.

I would like to thank my advisory committee member, Dr J. Kizito, Dr. A. Fernandez, and Dr. M Dhanasar. I would especially like to thank Dr. Frederick Ferguson for being my major professor. He has provided me with outstanding technical support. He also provided me with financial support through the graduate assistantship. I also thank Dr. M. Sundaresan for allowing me to use his research group's high performance computer.

I would like to thank my parents Dr Frank and Tamari Mrema. I would like to thank my siblings Helen and Jeremiah Mrema. Most of all, I would like to thank my wife Tasha Mrema for her love and care. Lastly, I would also like to thank my colleagues and classmates for going through this journey with me.

Table of Contents

List of Figures viii

List of Tables x

List of Symbols xi

Abstract 2

CHAPTER 1 Introduction 3

1.1 The Problem Statement 3

1.2 The Governing Equations 4

1.3 Motivation of Thesis 5

1.4 Objectives of Thesis 6

1.5 Thesis Outline 6

CHAPTER 2 Literature Review 8

2.1 Computational Fluid Dynamics Overview 8

2.3 CFD Schemes 9

2.3 An Abridged History of CFD 10

CHAPTER 3 Methodology 13

3.1 The Integral-Differential Scheme (IDS) Concepts 13

3.1.1 Objective. 13

3.1.2 The flow field domain. 14

3.1.3 IDS cell and control volume. 15

3.2 Utilization of the Conservational Laws 17

3.2.1 Application of the conservation of mass. 17

3.2.2 Application of the conservation of momentum. 20

3.2.3 Application of the conservation of energy. 28

3.2.4 Normalized form of the conservational equations. 35

3.3 The IDS Time Marching Methods 40

CHAPTER 4 Results and Discussion 44

4.1 Supersonic Flow over Rearward-Facing Step (RFS) Problem 45

4.1.1 RFS problem setup. 46

4.1.2 RFS problem boundary and initial conditions. 47

4.1.3 RFS problem results. 49

4.2 Supersonic Flow over Cavity 65

4.2.1 Cavity problem setup. 66

4.2.2 Cavity problem boundary and initial conditions. 67

4.2.3 Cavity problem results. 68

CHAPTER 5 Conclusion and Recommendations 77

5.1 Conclusion 77

5.2 Future Research Recommendation 79

References 80

List of Figures

Figure 3.1. A general discretized flow field domain. 14

Figure 3.2. (A) An IDS cell and (B) IDS control volume..... 15

Figure 3.3. Control volume with spatial, and temporal cell..... 17

Figure 3.4. Forces acting on a cell. 21

Figure 3.5. Shear stress stencil..... 25

Figure 3.6. The conservation of energy applied for a cell. 28

Figure 4.1. Diagram of RFS flow field features [27]..... 45

Figure 4.2. Computational RFS geometry [27]. 46

Figure 4.3. RFS computational domain with colored boundaries. 48

Figure 4.4. Solution convergence study..... 50

Figure 4.5. Grid convergence study. 51

Figure 4.6. The IDS pressure contour plot..... 52

Figure 4.7. The PLIIF pressure contour plot [21]. 52

Figure 4.8. The IDS pressure contour plot..... 54

Figure 4.9. The PLIIF temperature contour plot [21]. 55

Figure 4.10. Mach number contour plot with streamlines. 56

Figure 4.11. Mach number contour plot with streamlines (whole domain)..... 57

Figure 4.12. Comparison of IDS and experimental profiles at $x = 2.465Hstep$. 58

Figure 4.13. Comparison of IDS and experimental profiles at $x = 3.388Hstep$. 60

Figure 4.14. Comparison of IDS and experimental profiles at $x = 5.2208Hstep$. 62

Figure 4.15. Comparison of IDS and experimental profiles at $x = 6.465Hstep$. 63

Figure 4.16. Comparison of IDS and experimental profiles at $x = 10.155Hstep$. 64

Figure 4.17. Sketch of supersonic flow over cavity problem [22]..... 66

Figure 4.18 Computational cavity [22]..... 67

Figure 4.19. Computational domain and boundaries..... 68

Figure 4.20. Solution convergence study..... 69

Figure 4.21. Contour plots from IDS (A,B) and experimental flow visualization images(C) [22].

..... 70

Figure 4.22. Mach number (A) and velocity (B,C) contour plots..... 72

Figure 4.23. Streamlines comparison for IDS code (A) and VULCAN Navier-Stokes

code(B) [22]..... 74

Figure 4.24. Pressure distribution inside the cavity walls [22]..... 75

List of Tables

Table 4.1 Rearward-facing step problem Parameters 47

Table 4.2 RFS Boundary Conditions 49

Table 4.3 Supersonic Flow over Cavity Parameters 67

List of Symbols

ρ	Density
t	Time
$\forall$	Volume
$\bar{V}$	Velocity vector
$\bar{s}$	Surface vector
u	Velocity in the x-direction
v	Velocity in the y-direction
e	Total specific energy
T	Temperature
$\bar{q}$	Heat flux in the x-direction
P	Pressure
μ	Dynamic viscosity
λ	Second viscosity coefficient
$\hat{\tau}$	Friction stress tensor
τ_{xx}	Normal stress in the x direction
τ_{yy}	Normal stress in the y direction
τ_{xy}	Shear stress in the x direction exerted in a plane perpendicular to y direction
τ_{yx}	Shear stress in the y direction exerted in a plane perpendicular to x direction

k	Thermal conductivity
c_v	Specific heat measured at constant volume
U_m	Solution vector of Navier-Stokes equation
L_{ref}	Reference length
ρ_*	Dimensionless density
x_*	Dimensionless x-axis
y_*	Dimensionless y-axis
u_*	Dimensionless x-component of the velocity
v_*	Dimensionless y-component of the velocity
μ_*	Dimensionless Dynamic Viscosity
k_*	Dimensionless Thermal conductivity
T_*	Dimensionless temperature
ρ_∞	Density at freestream conditions
M_∞	Mach number at freestream conditions
p_∞	Pressure at freestream conditions
a_∞	Speed of sound at freestream conditions
u_∞	X-component of the velocity at freestream conditions
T_∞	Temperature at freestream conditions

Re_L	Reynolds number based on a characteristic length, L
Pr	Prandtl number
γ	Ratio of $\frac{C_p}{C_v}$
i_{max}	The number of grid cells in the x-direction
j_{max}	The number of grid cells in the y-direction
Δx	Step size in the x-direction
Δy	Step size in the y-direction
Δt	Time step
a	Speed of sound
C	Courant number in CFL criterion

Abstract

This MS Thesis seeks to validate the accuracy of the Integral-Differential Scheme (IDS). In the attempts to accomplish this task, research efforts were focused on the scheme's ability to capture the physics of known flow fields, as well as the scheme's ability to predict the features of flow field quantities that may be derived from experimental measurements. The IDS was developed with the goal of being computationally efficient, from a programming perspective, as well as being numerically accurate, stable, and robust, from a mathematical perspective. The IDS is designed to solve the full Navier-Stokes equations in their integral forms. Unlike traditional control volume schemes, the IDS is built upon two sets of cells: spatial and temporal cells. For 2-D flows, the IDS considers an elementary control volume as a collection of four spatial cells and a single temporal cell. Similar to other explicit CFD schemes, the IDS relies on the use of the Taylor series expansion and other traditional CFD criteria. It is of interest to note that there are previous IDS validation studies which were conducted at North Carolina A&T State University. These past studies mainly focused on the qualitative aspects of the flow field physics. Furthermore, in all cases, they focused on flow field problems that can be represented by single-block grids. In this analysis, the validation studies are focused on multi-block grids in which the physics of the flow field is made complicated due to the presence of shock waves and flow separation zones. Of interest to this MS Thesis are two supersonic flow field problems that are supported by experimental data; namely, the supersonic flow over a rearward-facing step problem and the supersonic flow over a cavity problem. The validation studies conducted herein demonstrated that the IDS was able to predict the experimental data in both cases.

CHAPTER 1

Introduction

For mankind to move towards global sustainability, it is vital for future technology to evolve towards economical, socially acceptable, and environmental friendly directions. A vast range of fields can contribute to this sustainable development. These fields include, but are not limited to, environmental engineering, meteorology, bio-medical, civil engineering, aeronautics, and astronautics. All these fields are directly or indirectly connected to fluid dynamics, heat transfer, phase changing fluids, and/or chemical reacting fluids. The mentioned phenomena can be modeled and simulated via Computational Fluid Dynamics (CFD). The ability to simulate the interaction between natural phenomena and man-made systems will allow engineers, researcher, innovators, and designers to utilize CFD as a means of developing systems to become more sustainable. Therefore, the advancement of CFD will ultimately lead to a more sustainable world [1-5]. This thesis focuses on improving the field computational fluid dynamics by validating a new innovative computational fluid dynamics scheme.

1.1 The Problem Statement

In a two-dimensional realm, consider a Newtonian fluid with no active body forces. This type of fluid can be modeled by the Navier-Stokes equations. The Navier-Stokes equations are nonlinear partial differential equations that describe the dynamics of a compressible, viscous, and unsteady flow. Equation 1.1-1.3 display the integral forms of the Navier-Stokes equations for the two dimensional case. The complexities of this system of equations have made it, at the current time, impossible to obtain analytical solutions. The most accurate way to obtain the solution to these equations is via the use numerical techniques. One of these numerical techniques is a CFD scheme known as the Integral-Differential Scheme (IDS). The IDS can be used solve the Navier-

Stokes equations. The IDS is supposed to be "simple, accurate, and a robust" scheme [6]. The goal of this thesis is to assess the credibility of the Integral-Differential Scheme by validating it.

1.2 The Governing Equations

The Navier-Stokes equations are governed by three principles that are derived from the Laws of physics:

1. Mass is conserved
2. Momentum is conserved (Newton's 2nd Law).
3. Energy is conserved.

These three principles can be modeling by mathematical equations. In this thesis, the integral form of the two-dimensional Navier-Stokes equations will be the governing mathematical model, Equations 1.1-3

$$\iiint_{\forall} \frac{\mathrm{d}\rho}{\mathrm{dt}} \mathrm{d}\forall + \oiint_{s} \rho\bar{\mathrm{V}} \cdot \mathrm{d}\bar{\mathrm{s}} = 0 \qquad (1.1)$$

$$\iiint_{\forall} \frac{\mathrm{d}(\rho\bar{\mathrm{V}})}{\mathrm{dt}} \mathrm{d}\forall + \oiint_{s} \rho\bar{\mathrm{V}}(\bar{\mathrm{V}} \cdot \mathrm{d}\bar{\mathrm{s}}) = -\oiint_{s} \mathrm{P}\mathrm{d}\bar{\mathrm{s}} + \oiint_{s} \hat{\tau} \cdot \mathrm{d}\bar{\mathrm{s}} \qquad (1.2)$$

$$\iiint_{\forall} \frac{d(\rho e)}{dt} d\forall + \oiint_{s} \rho e(\bar{V} \cdot d\bar{s}) = -\oiint_{s} P(\bar{V} \cdot d\bar{s}) + \oiint_{s} \bar{V} \cdot (\hat{\tau} \cdot d\bar{s}) + \oiint_{s} \bar{q} \cdot d\bar{s} \qquad (1.3)$$

In the continuity equation (Equation 1.1),the symbols $\rho, \bar{V}, t, \forall, \mathrm{s}$ represent density, velocity, time, volume, and surface, respectively. In the conservation of momentum equation (Equation 1.2), two additional new variables, pressure (P) and friction stress tensor ($\hat{\tau}$), have been introduced. In the conservation of energy equation (Equation 1.3), total specific energy (e) is added [7].

1.3 Motivation of Thesis

In the past four decades, the field of CFD has progressed at a very fast rate. CFD is now at a point where it can be used to analyze any man-made or natural system that has fluid involvement. This progress is largely due to the increase of powerful and affordable computers, and improvement in high fidelity models. With the increasing use of CFD, it is important for CFD reliability to increase as well. Verification, validation, and accuracy quantification address the issues of assessing the accuracy and reliability of CFD schemes [2]. Therefore, research in scheme validation, verification, and accuracy analysis is of interest to the CFD community.

Many of the current CFD commercial solvers require an experienced user for operations. The process of selecting the correct models (e.g. turbulence models, chemical reaction models) and generating grids require a certain level of expertise. This requirement limits the number of users that can use CFD effectively as a tool for research or industrial applications. Another limiting factor of current CFD solvers is the time requirement for setting up a CFD problem. A large portion of time is spent by a user to generate the grid system that is required by a CFD solver [8]. As the field of CFD evolves, the next-generation of CFD tools will need to be robust, user-friendly, accurate, and effective in the problem setup phase [5]. Under these pretenses, a new CFD scheme called the Integral-Differential Scheme (IDS) was developed. The new scheme was designed to meet the next generation requirement. Previous validations on the IDS were conducted on simple single block grids [6910]. This limited the number of complex flow fields that could be simulated by the boundary conditions. The IDS has yet to be validated on more complex domains, i.e. domains that can only be represented by multiple grid blocks. Therefore, the research efforts herein are motivated by the needs of the CFD community and the lack of the IDS validation studies on multi-block grids.

1.4 Objectives of Thesis

The purpose of this thesis is to assess the credibility of the Integral-Differential Scheme (IDS) by independently validating the scheme. In this analysis, the proposed validation process consists of a direct use of the IDS to solve problems that contain complex fluid dynamic interactions as well as those described by complex benchmark geometries. In efforts to achieve the proposed thesis goal, the following objectives were set:

- Update the current IDS code so that it can take and solve multi-block grids
- Use the IDS code to solve a 2-D supersonic flow over a Rearward-Facing Step problem
- Use the IDS code to solve a 2-D supersonic flow over an open cavity problem
- Validate the IDS by comparing the IDS code solutions to experimental data.

1.5 Thesis Outline

This thesis consists of five Chapters. Chapter 1, the current Chapter, describes the motivation behind this research effort as well as its objectives and its expected outcomes. Detail descriptions of this MS Thesis purpose, its motivation and its technical objectives are also presented. Chapter 2 summarizes the findings of an extensive literature survey that scanned the numerical analysis field for technical information relevant to this Thesis. In addition, Chapter 2 provides the readers with a rudimentary knowledge of CFD along with a comprehensive review of its development from a historic perspective. The third Chapter, Chapter 3, presents a review of the IDS solution methodology as it relates to the Navier-Stokes equations. In efforts to put the IDS in perspective and highlight its current challenges, a detail review of the scheme is provided. Chapter 4 discusses the two fluid dynamic problems of major interest to this Thesis, and the methods used in the IDS validation process. Moreover, Chapter 4 discusses, in great detail, the

results obtained from the implementation of the IDS code. Both, qualitatively and quantitatively descriptions of the fluid dynamic interactions identified in the IDS solutions files are presented. The results obtained from the IDS solution files along with those obtained from experimental observations are compared and analyzed. This MS thesis concludes with Chapter 5, in which, the current research efforts and their corresponding outcomes are summarized. Finally, based on the lessons learned and the new challenges identified, an appropriate set of research effort are identified and recommend as future work.

CHAPTER 2

Literature Review

In this chapter, a brief but pertinent technical overview of the field of CFD is presented. Following this overview, a discussion of the most frequently used CFD schemes of current fluid dynamists are presented and critically reviewed. Lastly, an abridge history of CFD is provided. The goal of this effort is to provide the readers with a clear perspective of CFD and the place the IDS hold in this technical space.

2.1 Computational Fluid Dynamics Overview

Computation Fluid Dynamics (CFD) is the analysis of systems involving fluid flow, heat transfer, chemical reactions, and other associated phenomena by means of computational simulation. Fluid dynamics is governed by fundamental principles, e.g. conservation of mass, conservation of momentum, and conservation of energy. These principles can be expressed by mathematical models, which are usually ordinary differential equations or partial differential equations. The ability to use numerical methods to solve these mathematical models constitutes the foundation of CFD. The use of CFD ranges from industrial applications to research applications. From the perspective of industry, CFD can be used to design, verify designs, and/or test designs. For example, CFD techniques have been utilized to design, research, and manufacture aircraft shapes, jet engines, and even combustion chamber. From the academic perspective, CFD can be used to research new phenomena, verify and validate experiments and/or theories. CFD has gained favor in a wide range of fields. This has resulted in CFD becoming a multidiscipline tool. For example, in marine engineering CFD has been used for studying loads on off-shore structures; in environmental engineering, CFD has been used to study distribution of pollutants; in meteorology, CFD has been used to weather predictions; and

in biomedical engineering, CFD has be used to study blood flows through arteries [8]. Overtime CFD has gained prominence and credibility to the point that it has become a separate branch of research in Engineering. As a result, there are now three main branches of research in engineering, pure theory and pure experiment, and computational fluid dynamics [7].

2.3 CFD Schemes

Generally, CFD programs consist of three main elements, pre-processor, solver, and post-processor. The pre-processing consists of defining and setting up the flow problem to the CFD program. During this phase, the geometry of the region of interest is defined by discrete points. This region of interest is known as the domain. The system of discrete points is known as a grid (or mesh). The grid points form cells (or control volumes). The process of forming grid system is known as grid generation. The solution of the flow problem is obtained when the flow field properties (velocity, pressure, temperature etc.) are known at discrete locations across the domain. These discrete locations are known as nodes. Depending on the scheme, nodes may be inside the cells (cell centered) or they may coincide with the discrete points (vertex centered). Pre-processing also involves defining the fluid properties, specifying the boundary and initial conditions, and specifying the physical and chemical phenomena models. With most CFD projects, over 50% of the time is spent on the preprocessing phase [8]. The time spent on grid generation is a major drawback.

The CFD solver is the program used to obtain the solution for a particular fluid problem. The algorithms used by the CFD solver are based on CFD scheme that are designed to numerically evaluate the flow field solution. There are many numerical solution techniques. The most prominent numerical solution techniques are finite difference, finite element, and spectral method. This thesis focuses of a CFD scheme that is based on the control volume method. The

control volume method can be derived from the finite difference and the finite element method. The control volume method consists of integration of the governing equations over the elementary control volumes, conversion of the integrals into their algebraic forms, and finally using some iterative method to obtain a solution. The control volume method is distinguished from the other methods by its integration step. The final phase of CFD application is the post-processing. This phase consists of displaying and analyzing the final solution [8] .

2.3 An Abridged History of CFD

The foundations of Computational Fluid Dynamics began to get formed in the early 1900s. Efforts by Richardson, Courant, Friedrichs, Lewy, Southweel, von Neumann, Lax and Godunov addressed fundamental issues in numerical analysis that would eventually be encountered by CFD [11]. CFD has developed in parallel to the evolution of high performance computers. Initially the incentive of CFD was to solve problems related to national defense. Overtime the discipline has spread to scientific and engineering applications [12]. The first major use of CFD occurred in 1947. Kopal used numerical methods to compile aerodynamic properties table of supersonic flow over sharp cones. His work was conducted on primitive digital computer at Massachusetts Institute of Technology [13]. In the 1950's and early 1960's was the advent of high-speed computers. Many of the prolific methods during this period were developed by the Fluid Dynamics Group (T-3) led by F. H. Harlow at Los Alamos national Laboratory [1214]. During this period marks the 1st generation CFD methods. The CFD methods were mainly used to tackle high velocity flows [913]. One of the 1st generation schemes, that were used to solve flow problems, was the Particle-In-Cell (PIC) method. The scheme was proposed by Harlow (1957) and it was designed for transient, compressible flow problems. The scheme was plagued by its intensive memory and computational requirement [3]. In 1959

Godunov used the upwind scheme to solve the Euler equations. He also developed an ingenious interpretation of the upwind scheme [15]. Gentry et al. (1966) developed an alternate method known as the Fluid-In-Cell (FLIC) method, which used finite differencing in Eulerian approach. FLIC method had stability issues due to improper velocity and pressure coupling. Harlow and Welch formed the Marker-And-Cell (MAC) method (1965). The MAC method successfully simulated unsteady incompressible flows using primitive variables and staggered grids [3]. Lax and Wendroff are the pioneers of explicitly marching techniques. Using Taylor series expansion, they managed to develop a second-order accurate in space and time; however, the scheme used intensive manipulations to obtain the second order accuracy in time [6]. In 1969, MacCormack introduced a two-step solution scheme. The MacCormack method is the most popular explicit finite-differencing scheme. It is a simpler variant of the Lax-Wendroff method. The scheme became known as the predictor-corrector method. The MacCormack Scheme is an explicit scheme with second-order accurate space and time discretization. The MacCormack method was applied to solve the compressible Navier-Stokes equations [16].

The second generation of CFD broke through during the 1970s. During this period, the orthogonal surface-fitted structured grids were introduced. The advancement of computational resources allowed the CFD studies to tackle more practical problems such as air flow over airfoils [916]. Between 1977 and 1997 Bram Van Leer et al. worked on several versions of the upwind differencing. It was observed then that the upwind schemes presented artificial viscosity errors [6].

In the previous paragraphs, a brief review of the history of CFD schemes was given. In actuality, there are great numbers of CFD schemes that have been developed since the 1940s.

More information can be found from text books by Anderson [16], Chung [17], Versteeg and Malalasekera [8].

CHAPTER 3

Methodology

Documented in this chapter is a generalized discussion of the IDS and its direct application to the solution of the Navier-Stokes equations. The so-called IDS, explicitly known as the Integral-Differential Scheme, is based on the finite control volume approach to solving the conservation laws. The scheme was initially introduced by Dr. Gafar Elamin [618]. In addition, the scheme was developed with the goal of providing a straight forward and robust programming concept to solve the Navier-Stokes equations without losing any numerical accuracy in the process. For a detailed insight of the scheme, the readers are referred to Dr. Elamin's MS thesis and Ph.D. dissertation [618]. Nevertheless, in efforts to put this MS thesis in perspective, a brief review of the scheme is warranted, and is therefore provide herein.

3.1 The Integral-Differential Scheme (IDS) Concepts

3.1.1 Objective. The beauty of the IDS lies in the fact that the scheme is simple to program, user-friendly, and focused on capturing the physics of the flow field. The scheme solves the integral form of the Navier-Stokes Equations, equations 1.1-3. These equations are referred to as the governing equations. In its evaluation process, IDS operates with conserved quantities ($\rho, u\rho, v\rho, e$), as opposed to the primitive variables (u, v, T, p). This approach guarantees the flux quantities ($\rho, u\rho, v\rho, e$) are conserved throughout the whole domain and the governing equations are not violated.

On a local level, fluxes are accounted for in each of the elementary control volumes. In order to utilize the conservational laws, the governing equations are converted from their integral forms into their algebraic forms. This conversion is made possible by using the mean value theorem. The algebraic relations relate the time rate change of the flux quantities with the local

flow field properties. Essentially, the time derivative of the flux quantities is evaluated based on the flow field information. To ensure accuracy, a wide range of nodes are used to evaluate the time derivative of the flux quantities. This approach allows the scheme to be able to capture areas of high-gradients, such as a shock region. Lastly, the scheme uses consistent averaging of node variables when updating the solution. This approach forces the IDS to have a very unique and involved elementary control volume. A more detailed explanation of the scheme will be given in the upcoming sections.

3.1.2 The flow field domain. In order to begin the IDS, the flow field domain needs to first get discretized. Figure 3.1 displays a typical flow field domain.

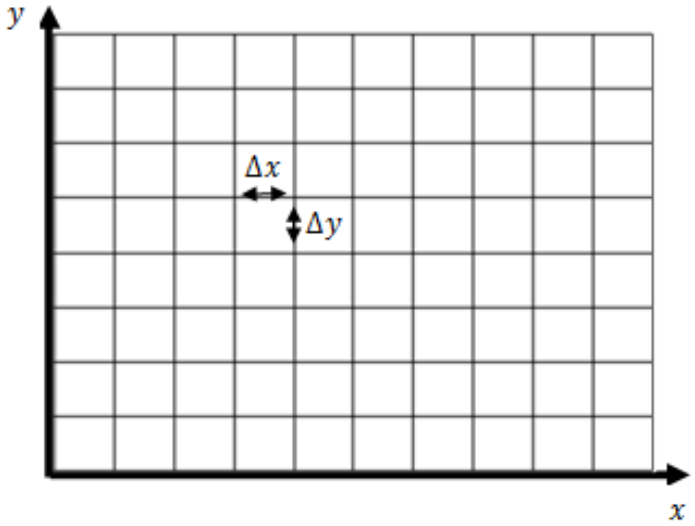

Figure 3.1. A general discretized flow field domain.

The continuous physical flow field is divided into discrete points that hold the aerodynamic properties (velocity, pressure, temperature, density etc.) of the given region. Each of these nodes is evenly separated by a distance of Δx and Δy, as shown in Figure 3.1. The IDS cells have nodes at the vertices, as opposed to having cell centered nodes. This means that any given cell is defined by four nodes for a two dimensional problem and eight nodes for a three dimensional problem. This thesis focuses on a two dimensional flow fields.

When working with a 2-D system, the value of Δz is assumed to be equal to 1 unit. Thus, the volume of a cell is$(\Delta x)(\Delta y)(1)$, while the surface area of a cell is $(2\Delta x + 2\Delta y)(1)$. For convenience, Δz values will not be explicitly written in any of the equations. Lastly, it is also assumed that there are no variations in properties in the z-direction. For the convenience of this thesis, all z-direction equations or properties will not be mentioned.

3.1.3 IDS cell and control volume. The IDS uses elementary control volumes that are composed of cells. Figure 3.2 displays a cell (A) and a control volume (B).

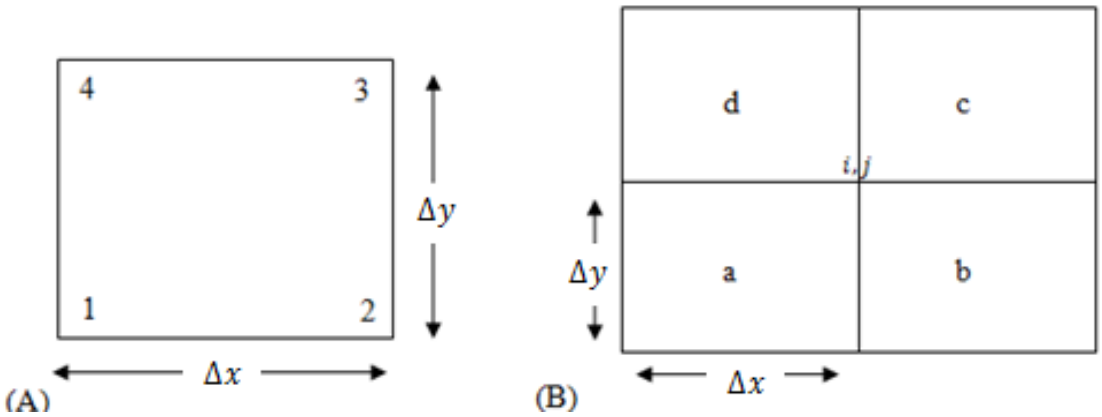

Figure 3.2. (A) An IDS cell and (B) IDS control volume.

In Figure 3.2, the dimension of a cell is $\Delta x \times \Delta y$. Each of the cells is defined by 4 nodes, as labeled in the figure. The flow field properties are defined at each node, i.e. cell vertices. Notice that the center of the cell does not correspond to a discrete node. The importance of the imaginary center node will be further discussed in the following sections.

The governing equations are applied to the cells in order to obtain the temporal flux of the cells. The governing equations are composed of volume and surface integrals, see equation 1.1-3. The volume integral terms cannot be explicitly evaluated because information within a given cell is not known. However, the surface integral can be evaluated because the surface information can be interpolated from the information at the cell vertices (nodes). The volume

integral can be evaluated implicitly. This is accomplished by isolating the volume integrals and evaluating the surface integrals terms. Once the volume integral is known, the temporal flux can be extracted by using the mean value theorem. The temporal flux that is calculated for a given cell is only applicable for the center of that cell. This is significant because the center of a cell does not correspond to a node location. This cell center corresponds to an imaginary node. As a result, individual cells cannot be used to update a node point. To resolve this issue, the IDS introduce the concept of a control volume.

In the IDS, the shape of the control volume is defined by 4 cells, as shown in Figure 3.2 (B). The four cells are known as spatial cells. Each control volume is identified by the indices i, j. In a given control volume, the spatial cells are locally identified as $a, b, c,$ or d, depending on their locations. Figure 3.2 (B) displays the control volume and its cells identities. Note that the center of a control volume lies directly on a mesh point (cell vertex). This is imperative to understand because the time derivative that is calculated for a spatial cell is only applicable for the center of the cell (imaginary node). Control volumes, on the other hand, can update a mesh point since their centers correspond to a node. To update a node, an arithmetic averaged of temporal fluxes is used. This averaged temporal flux is obtained from the temporal flux of the four spatial cells within the control volume. Thus, the temporal flux of a control volume is equivalent to the average of the temporal flux of all its spatial cells.

In addition to the IDS control volume and spatial cell, there is another cell known as the temporal cell. A control volume has one temporal cell. The temporal derivatives that are located at the local center of the four spatial cells form the vertices of the temporal cell. Figure 3.3 displays a control volume with the spatial cells labeled a,b,c,d, and the temporal cell highlighted with light blue cross patterns.

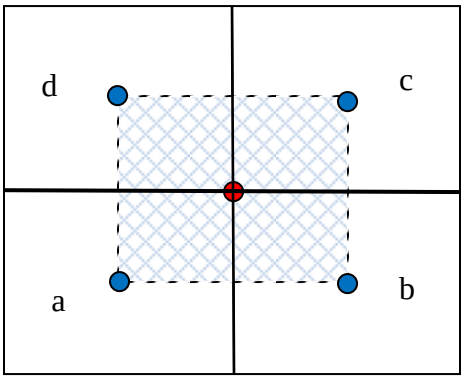

Figure 3.3. Control volume with spatial, and temporal cell.

As the Figure 3.3 shows, the center of each spatial cell corresponds to a vertex of the temporal cell. Consequently, the center of the temporal cell aligns with the center of the control volume. This alignment allows the control volume to use the average time rate change of fluxes given by the temporal cell, to update the solution as the scheme marches forward in time.

3.2 Utilization of the Conservational Laws

At this point, a description of the IDS control volume, spatial cells, temporal has been given. However, a detailed discussion on the governing equations evaluation process is lacking. The following section will provide an explanation on how the temporal fluxes are evaluated from the governing equation. The application of the conservation of mass, momentum, and energy will be discussed in the following sections respectively.

3.2.1 Application of the conservation of mass. Equation (3.1) shows the integral form of the conservation of mass. From the conservation of mass, it is known that the net flow rated out of the system is equivalent to the time rate decrease of mass within the system. This principle can be modeled by Equation 3.1. In Equation 3.1, the symbols, $\rho, \bar{V}, t, \forall,$ s, represent density, velocity, time, volume, and surface respectively. The first integral is integrated over the entire volume. The second integral is integrated over the surface. Keep in mind, this thesis focuses on

2-D derivations. Thus, the z-direction values and properties influences are ignored. Furthermore, for a 2-D Cartesian system $\bar{V} = u\,\hat{\imath} + v\,\hat{\jmath}$ and $\bar{s} = dy\,\hat{\imath} + dx\,\hat{\jmath}$.

$$\iiint_{\forall} \frac{d\rho}{dt} d\forall + \oiint_{S} \rho \bar{V} \cdot d\bar{s} = 0 \qquad (3.\ 1)$$

Pictorially, Equation 3. 1 can be represented by Figure 3.4, where the mass flow moving in and out of the cell is shown by the arrows.

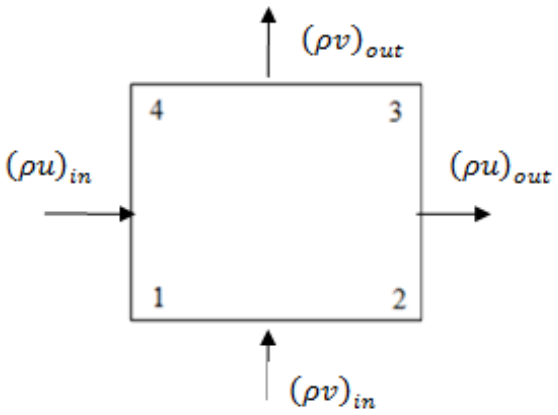

Figure 3.4. Conservation of Mass in a Cell.

From Figure 3.4, the mass flux at each face can be interpolated based on the information known at the cell nodes. As the cell dimension decreases, this interpolation becomes more accurate.

For the IDS, it is of interest to obtain the time rate decrease of mass within the system. Note that the fluxes at the surfaces can be obtained explicitly since the flow field properties are known at the nodes. The temporal flux can be extracted from the volume integral. The volume integral is inversely related to the surface integral. Therefore, two steps are needed to access the temporal flux of the system. The first step is to evaluate the surface integral. The second step is to extract the temporal flux from the volume integral.

To evaluate the surface and the volume integral, the mean value theorem is used. The mean value theorem can be stated as following: the integral of a function $f(x)$ that is continuous between (a, b) is equal to the average value of $f(x)$ between (a, b) multiplied by the difference between a and b. The expression is displayed in Equation 3.4.

$$\int_a^b f(x)dx = f_{a-b}^{mean}(b-a) \tag{3. 2}$$

Before evaluating the surface integral, the surface integral is separated so that each face can be evaluated individually, see Equation 3.3. The surface vector always points away from the surface. As a result, the left and bottom face integrals are negative.

$$\oiint_s \rho\bar{V}\cdot d\bar{s} = \int_{right}(\rho u)\,dy - \int_{left}(\rho u)\,dy + \int_{up}(\rho v)\,dx - \int_{down}(\rho v)\,dx \tag{3. 3}$$

The mean value theorem can now be applied to integrals on the right hand side of Equation 3.3. This operation will result in Equation 3.4. Notice that for a given cell face, the mass flow rate in or out is equal to the average mass flow rate of the two nodes adjacent to that face.

$$\begin{aligned}\oiint_s \rho\bar{V}\cdot d\bar{s} = {} & \frac{(\rho u)_1 + (\rho u)_4}{2}\Delta y - \frac{(\rho u)_2 + (\rho u)_3}{2}\Delta y + \frac{(\rho v)_3 + (\rho v)_4}{2}\Delta x \\ & - \frac{(\rho v)_1 + (\rho v)_2}{2}\Delta x\end{aligned} \tag{3. 4}$$

The second step is the extraction of the temporal flux from the volume integral, see Equation 3.1. This is accomplished by using the mean value theorem again. The resulting form of the volume integral after applying the mean value theorem is shown in Equation 3.5. The quantity represented by the symbol $\left(\frac{d\rho}{dt}\right)_{cell}^{avg}$ is the time rate change of density within the cell. Since the domain is discrete, the temporal flux is linked with the imaginary node at the center of the cell.

$$\iiint_{\forall} \frac{d\rho}{dt} d\forall = \left(\frac{d\rho}{dt}\right)_{cell}^{avg} \Delta x \Delta y \qquad (3.5)$$

Using Equations 3.4 and 3.5, one can isolate the temporal flux when it is applied in Equation 3.1. Equation 3.6 exhibits this new algebraic relation. Note that in Equation 3.6, the surface integral has been moved to the right hand side. Additionally, the cell volume has been divided from the right hand and left hand side of the equation; thus, completely isolating the time rate change of density.

$$\left(\frac{d\rho}{dt}\right)_{cell}^{avg} = \frac{(\rho u)_1 + (\rho u)_4}{2\Delta x} - \frac{(\rho u)_2 + (\rho u)_3}{2\Delta x} + \frac{(\rho v)_3 + (\rho v)_4}{2\Delta y} - \frac{(\rho v)_1 + (\rho v)_2}{2\Delta y} \qquad (3.6)$$

In Equation 3.6 the information on the right hand side is provided by the spatial cell. Thus, using spatial cell, a temporal cell vertex can be calculated.

3.2.2 Application of the conservation of momentum. The conservation of momentum principle is based on Newton's second law of motion. According to the principle, " The net force acting on a fluid particle is equal to the time rate of change of the linear momentum of the fluid particle" [19]. In this thesis, the acting forces that are considered are caused by pressure, normal stress, and shear stress. Gravitational force, electro-magnetic forces, and any other force are neglected. The forces acting on a cell are illustrated in Figure 3.5. The forces due to pressure are always compressing the cell; thus, the pressure forces are compressive forces. Conversely, the forces due to normal stress can be compressive or tension forces. The forces due to shear stress are more commonly called friction. Therefore, viscous flows have high shear stress. On the other hand, the forces due to normal stress affect the compressibility of the flow. Flow fields that are highly compressible, have high activity with the normal stress. The combination of shear stress and normal stress form the friction tensor.

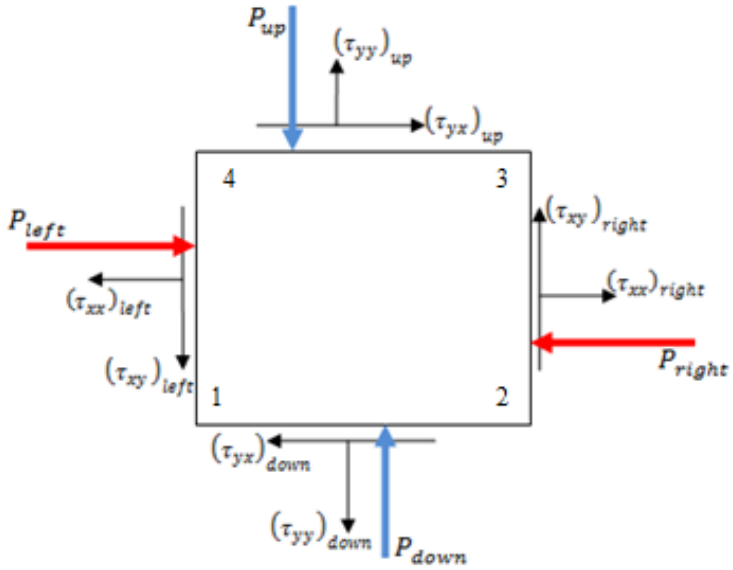

Figure 3.4. Forces acting on a cell.

The mathematical expression of the conservation of momentum is displayed in Equation 3.7. Equation 3.7 introduces two additional variables, pressure (P) and friction stress tensor ($\hat{\tau}$).

$$\iiint_{\forall} \frac{d(\rho\bar{V})}{dt} d\forall + \oiint_{S} \rho\bar{V}(\bar{V}\cdot d\bar{s}) = -\oiint_{S} P d\bar{s} + \oiint_{S} \hat{\tau}\cdot d\bar{s} \qquad (3.7)$$

The first term on the left hand side of Equation 3.7 is the time rate change of momentum in the cell. The second term is the momentum flux across the cell surface. On the right hand side, the first term is the Pressure force acting on the surface of the cell. The last term represents the viscous and compressible forces acting on the surface of the cell. The friction stress tensor components are shown in Equation 3.8, where the symbols $\tau_{xx}, \tau_{xy}, \tau_{yx}, \tau_{yy}$ are the shear stress and normal stress components.

$$\hat{\tau} = \begin{bmatrix} \tau_{xx} & \tau_{xy} \\ \tau_{yx} & \tau_{yy} \end{bmatrix} \qquad (3.8)$$

The momentum equation (Equation 3.7) is a vector equation. This equation could be separated into its individual vector components. The first component is in the x-direction and the second

component is in the y-direction. The x-momentum equation is shown in Equation 3.9. The y-momentum equation is shown in Equation 3.10.

$$\iiint_{\forall} \frac{d(\rho u)}{dt} d\forall + \oiint_{s} \rho u(\bar{V} \cdot d\bar{s}) = \int_{left} P\, dy - \int_{right} P\, dy + \int_{right} \tau_{xx}\, dy - \int_{left} \tau_{xx}\, dy + \int_{up} \tau_{xy}\, dx - \int_{down} \tau_{xy}\, dx \qquad (3.9)$$

$$\iiint_{\forall} \frac{d(\rho v)}{dt} d\forall + \oiint_{s} \rho v(\bar{V} \cdot d\bar{s}) = \int_{down} P\, dx - \int_{up} P\, dx + \int_{up} \tau_{yy}\, dx - \int_{down} \tau_{yy} dx + \int_{right} \tau_{yx}\, dy - \int_{left} \tau_{yx}\, dy \qquad (3.10)$$

The next step is to convert Equation 3.9 and 3.10 into their algebraic counterparts. The process of converting the x-momentum equation to its algebraic counterpart is the same as the process used for the y-momentum equation. For convenience, only the x-momentum equation will be converted step by step. At the end, the algebraic counterparts, for both the x-momentum and y-momentum equations, will be presented.

The process of converting the left hand side of x-momentum equation (Equation 3.9) is identical to the process used to convert the left hand side of the conservation of mass equation (Equation 3.1). The converted volume and surface will be identical to Equation 3.5 and Equation 3.4, respectively. The main difference will be that instead of having density (ρ) , the algebraic

forms would have mass flux (ρu). For the volume integral, the algebraic form would appear as 3.11. The surface integral, on the other hand, will appear as Equation 3.12.

$$\iiint_{\forall} \frac{d(\rho u)}{dt} d\forall = \left(\frac{\partial(\rho u)}{\partial t}\right)_{cell}^{avg} \Delta x \Delta y \tag{3. 11}$$

$$\oiint_{s} \rho u \bar{V} \cdot d\bar{s} = \frac{(\rho u^2)_1 + (\rho u^2)_4}{2} \Delta y - \frac{(\rho u^2)_2 + (\rho u^2)_3}{2} \Delta y + \frac{(\rho u v)_3 + (\rho u v)_4}{2} \Delta x - \frac{(\rho u v)_1 + (\rho u v)_2}{2} \Delta x \tag{3. 12}$$

The terms on the right hand side of equation 3.9 can be converted by invoking the mean value theorem first. For the pressure terms, the average pressure is calculated based on the pressure at the nodes of the corresponding face. Equation 3.13 shows this new converted net pressure force term.

$$\int_{left} P\, dy - \int_{right} P\, dy = \left(\frac{(P_1 + P_4)}{2}\right) \Delta y - \left(\frac{(P_2 + P_3)}{2}\right) \Delta y \tag{3. 13}$$

The friction stress force terms are more involved compared to the pressure terms. The first objective is to convert the terms to their algebraic counterpart. The resulting algebraic form of the normal stress and shear stress integrals for the x-direction momentum equation is shown in Equations 3.14-3.15.

$$\int_{right} \tau_{xx}\, dy - \int_{left} \tau_{xx}\, dy = (\tau_{xx})_r^{avg} \Delta y - (\tau_{xx})_l^{avg} \Delta y \tag{3. 14}$$

$$\int_{up} \tau_{xy}\, dx - \int_{down} \tau_{xy}\, dx = (\tau_{xy})_u^{avg} \Delta x - (\tau_{xy})_d^{avg} \Delta x \tag{3. 15}$$

For Newtonian fluids, shear stress is proportional to the time rate of strain (velocity gradients). Based on George Stokes's works, the friction stress tensor components can be shown to be equal to Equations 3.16-3.18, where μ represents the molecular viscosity coefficient and λ is the second viscosity coefficient [7]. To decrease the number of unknown variables, Stokes hypothesis is used to relate second viscosity coefficient to molecular viscosity coefficient. Stokes hypothesis provides the following relationship, $\lambda = -\frac{2}{3}\mu$.

$$\tau_{xx} = \lambda(\nabla \cdot \bar{V}) + 2\mu\frac{\partial u}{\partial x} = \lambda\left(\frac{\partial u}{\partial x} + \frac{\partial v}{\partial y}\right) + 2\mu\frac{\partial u}{\partial x} \qquad (3.16)$$

$$\tau_{yy} = \lambda(\nabla \cdot \bar{V}) + 2\mu\frac{dv}{dy} = \lambda\left(\frac{\partial u}{\partial x} + \frac{\partial v}{\partial y}\right) + 2\mu\frac{dv}{dy} \qquad (3.17)$$

$$\tau_{xy} = \tau_{yx} = \mu\left[\frac{\partial v}{\partial x} + \frac{\partial u}{\partial y}\right] \qquad (3.18)$$

In cases where the fluid is a calorically perfect gas, Sutherland's law can be used to relate viscosity to temperature, as shown in Equation 3.19 [7]. In the expression, the subscript r represents reference properties.

$$\mu = \mu_r\left(\frac{T}{T_r}\right)^{3/2}\frac{T_r + 110}{T + 110} \qquad (3.19)$$

The normal and shear stresses are functions of velocity gradient, which are evaluated at the surface. This brings the issue of how to represent the velocity gradients at the surfaces. The solution is to extend the stencil to include neighboring cells. Figure 3.6 represents the new stencil that will be used to evaluate the shear stresses at the cell boundaries. Notice the addition of the neighboring nodes $1_l, 4_l, 1_d, 2_d, 2_r, 3_r, 3_u, 4_u$ where the subscripts l, d, r, u represents left, down, right, and up, respectively.

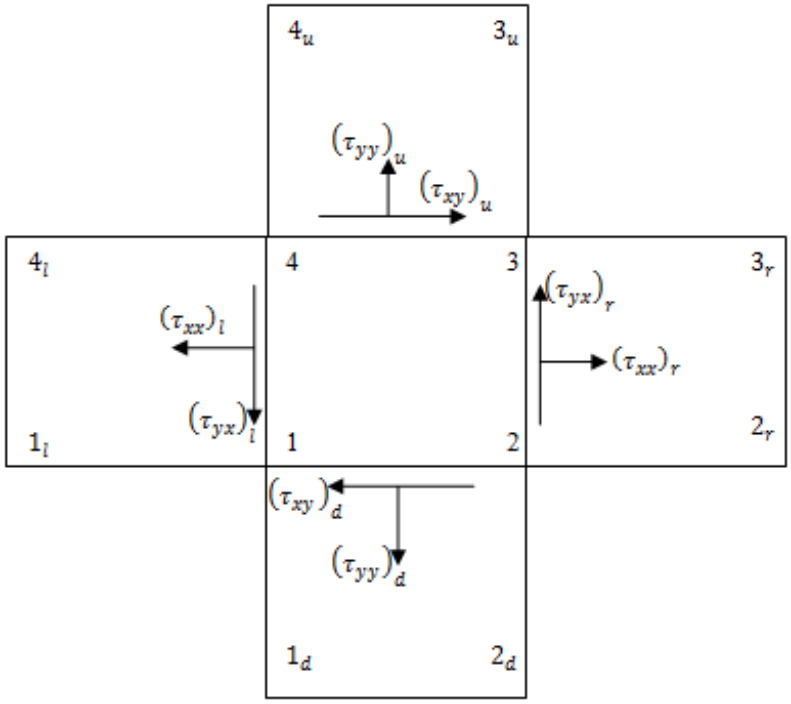

Figure 3.5. Shear stress stencil.

With this extended stencil, the velocity gradients are calculated by using the cell nodes and the neighboring nodes. For illustrations, the gradients associated with the left face of the cell are shown in Equations 3.20-23. The derivatives that are normal to the face require the use of their neighboring nodes. For example, in Equation 3.20-21, the derivatives with respect to the x-direction ($\frac{\partial}{\partial \mathrm{x}}$) are normal to the left face. As a result, the neighboring nodes, node 1_l and node 4_l, are used in the evaluation. On the other hand, the derivatives with respect to the y-direction (Equation 3.22-23) are parallel to the left face. This allows for one to use the face nodes, node 1 and node 4, when calculating $\frac{\partial}{\partial y}$. The gradients components for the other cell faces can be calculated in a similar manner as the gradients that are shown in Equation 3.20-23.

$$\left(\frac{\partial u}{\partial x}\right)_l = \frac{\left[\frac{1}{2}(u_1 + u_4) - \frac{1}{2}(u_{1_l} + u_{4_l})\right]}{\Delta x} \qquad (3.\ 20)$$

$$\left(\frac{\partial v}{\partial x}\right)_l = \frac{\left[\frac{1}{2}(v_1 + v_4) - \frac{1}{2}\left(v_{1_l} + v_{4_l}\right)\right]}{\Delta x} \quad (3.\ 21)$$

$$\left(\frac{\partial \mathrm{u}}{\partial \mathrm{y}}\right)_{\mathrm{l}} = \frac{(\mathrm{u}_4 - \mathrm{u}_1)}{\Delta \mathrm{y}} \quad (3.\ 22)$$

$$\left(\frac{\partial \mathrm{v}}{\partial \mathrm{y}}\right)_{\mathrm{l}} = \frac{(\mathrm{v}_4 - \mathrm{v}_1)}{\Delta \mathrm{y}} \quad (3.\ 23)$$

An important fact to note is that the lower face and left face of the cells use backward differencing techniques while the upper and right faces use forward differencing techniques. This convention, however, does not apply to cells that are next to the boundaries. When the derivatives are calculated for the cell faces that are next to the boundaries, the convention is reversed. That is to say the lower and left face of the cell use forward differencing techniques while the upper and right face use backward differencing techniques.

With the ability to obtain the velocity gradients, the shear and normal stress integral can be solved. For illustration purposes, Equation 3.22 and 3.23 displays theτ_{xx}, τ_{xy}, τ_{yx} for the left face of the cell. It must be mentioned that when μ_l is calculated, the temperature that is used is based on the average temperature between node 1 and node 4, $T_l = \frac{(T_1 + T_4)}{2}$.

$$(\tau_{xx})_l^{avg} = \frac{2}{3}\mu_l \left[2\left(\frac{\partial u}{\partial x}\right)_l - \left(\frac{\partial v}{\partial y}\right)_l\right] \quad (3.\ 24)$$

$$\left(\tau_{xy}\right)_u^{avg} = \left(\tau_{yx}\right)_l^{avg} = \mu_l \left[\left(\frac{\partial v}{\partial x}\right)_l + \left(\frac{\partial u}{\partial y}\right)_l\right] \quad (3.\ 25)$$

The conservation of momentum equation in the x-direction is completely converted once Equation 3.11-15, is substituted into Equation 3.9. The resulting new algebraic form is expressed in Equation 3.26. For convenience the "avg." superscript was dropped from the stress terms.

$$\left(\frac{\partial(\rho u)}{\partial t}\right)_{cell}^{avg}\Delta x\Delta y$$

$$= -\frac{1}{2}\Delta y\{[(\rho u^2)_1 + (\rho u^2)_4] - [(\rho u^2)_2 + (\rho u^2)_3]\}$$

$$-\frac{1}{2}\Delta x\{[(\rho uv)_1 + (\rho uv)_4] - [(\rho uv)_2 + (\rho uv)_3]\} \qquad (3.\ 26)$$

$$+\left[\left(\frac{(P_1 + P_4)}{2}\right) - \left(\frac{(P_2 + P_3)}{2}\right)\right]\Delta y + [(\tau_{xx})_r\ - (\tau_{xx})_l]\Delta y$$

$$+\left[\left(\tau_{xy}\right)_u - \left(\tau_{xy}\right)_d\right]\Delta x$$

Equation 3.26 is then rearranged to isolate the time rated change of x-momentum. This operation yields Equation 3.27.

$$\left(\frac{\partial(\rho u)}{\partial t}\right)_{cell}^{avg} = -\frac{\{[(\rho u^2)_1 + (\rho u^2)_4] - [(\rho u^2)_2 + (\rho u^2)_3]\}}{2\Delta x}$$

$$-\frac{\{[(\rho uv)_1 + (\rho uv)_4] - [(\rho uv)_2 + (\rho uv)_3]\}}{2\Delta y} \qquad (3.\ 27)$$

$$+\frac{[(P_1 + P_4) - (P_2 + P_3)]}{2\Delta x} + \frac{[(\tau_{xx})_r\ - (\tau_{xx})_l]}{\Delta x} + \frac{\left[\left(\tau_{xy}\right)_u - \left(\tau_{xy}\right)_d\right]}{\Delta y}$$

In a similar manner, the time rated change of y-momentum is displayed in Equation 3.28.

$$\left(\frac{\partial(\rho v)}{\partial t}\right)_{cell}^{avg} = -\frac{\{[(\rho v^2)_3 + (\rho v^2)_4] - [(\rho v^2)_2 + (\rho v^2)_1]\}}{2\Delta y}$$

$$-\frac{\{[(\rho uv)_3 + (\rho uv)_4] - [(\rho uv)_2 + (\rho uv)_1]\}}{2\Delta x} \qquad (3.\ 28)$$

$$+\frac{[(P_1 + P_2) - (P_4 + P_3)]}{2\Delta y} + \frac{\left[\left(\tau_{yy}\right)_u\ - \left(\tau_{yy}\right)_d\right]}{\Delta y} + \frac{\left[\left(\tau_{yx}\right)_r - \left(\tau_{yx}\right)_l\right]}{\Delta x}$$

Equations 3.27 and 3.28 are the final form of the equations that are used to evaluate the time rate change of momentum.

3.2.3 Application of the conservation of energy. The energy equation is derived from the 1st law of thermodynamics. The principle states that the total rate of change of energy in a system equals to the rate of heat added to the system and the rate of work done on the system [8]. In the IDS, the system is represented by a fluid cell. In the analysis, the heat added to the fluid cell is due to heat conduction. The work contributed to the cell is due to pressure and friction stress tensor. Figure 3.6 shows how the conservation of energy is applied for a cell. The new variable q represents heat addition.

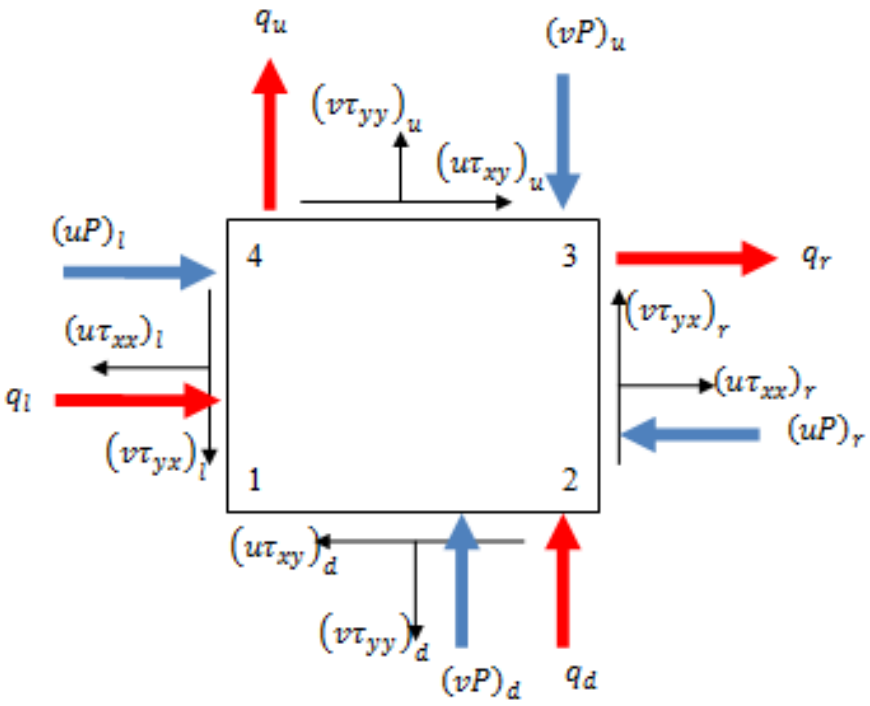

Figure 3.6. The conservation of energy applied for a cell.

The integral form of the conservation of energy equation is displayed in Equation 3.29, where e is the total energy per unit mass

$$\iiint_{\forall} \frac{d(\rho e)}{dt} d\forall + \oiint_{S} \rho e(\bar{V} \cdot d\bar{s}) = -\oiint_{S} P(\bar{V} \cdot d\bar{s}) + \oiint_{S} \bar{V} \cdot (\hat{\tau} \cdot d\bar{s}) + \oiint_{S} \bar{q} \cdot d\bar{s} \qquad (3.29)$$

As in the previous conservational equations, the left hand side has the temporal flux term and the spatial flux term. On the right hand side, the first term represents work due to pressure, the second term represents work due to stress, and the last term is the heat addition in the cell.

In this thesis, the total energy is composed of internal energy due to molecular motion and kinetic energy. For a calorically perfect gas, the internal energy of a gas can be assumed to be a linear function of temperature. The relationship is expressed by $u_{intenal} = c_v T$, where c_v is the specific heat that is measured at a constant volume. This expression is used to relate internal energy with temperature and specific heat. The final expression for the total energy per mass is $e = \mathrm{c}_v \mathrm{T} + \frac{u^2+v^2}{2}$.

The first objective, as in the previous conservational laws, is to convert the energy equation into its algebraic counterpart. Starting from the left hand side of Equation 3.29, the temporal integral and the spatial flux integral term can be transformed in the same manner as the temporal and spatial flux integrals in the mass and momentum equations. The conversion yields equations 3.30 and 3.31.

$$\iiint_{\forall} \frac{d(\rho e)}{dt} d\forall = \left(\frac{d(\rho e)}{dt}\right)_{cell}^{avg} \Delta x \Delta y \qquad (3.30)$$

$$\oiint_s \rho e(\bar{V} \cdot d\bar{s}) = \frac{[(\rho eu)_1 + (\rho eu)_4]}{2}\Delta y - \frac{[(\rho eu)_2 + (\rho eu)_3]}{2}\Delta y + \frac{[(\rho ev)_1 + (\rho ev)_2]}{2}\Delta x - \frac{[(\rho ev)_4 + (\rho ev)_3]}{2}\Delta x \quad (3.31)$$

The conversion process for the terms on the right hand side of equation 3.29 is more unique. The surface integrals are converted to their algebraic form via the use of the mean value theorem. The net work contributed by pressure forces is expressed in the following form:

$$\oiint_s P(\bar{V} \cdot d\bar{s}) = \frac{[(Pu)_1 + (Pu)_4]}{2}\Delta y - \frac{[(Pu)_2 + (Pu)_3]}{2}\Delta y + \frac{[(Pv)_1 + (Pv)_2]}{2}\Delta x - \frac{[(Pv)_4 + (Pv)_3]}{2}\Delta x \quad (3.32)$$

The work done by viscous forces are represented by the stress surface integral, $\oiint_s \bar{V} \cdot (\hat{\tau} \cdot d\bar{s})$. The surface integral is applied to each surface individually. This operation results in the following form of the stress surface integral:

$$\oiint_s \bar{V} \cdot (\hat{\tau} \cdot d\bar{s}) = \int_{right} u\tau_{xx} dy - \int_{left} u\tau_{xx}\, dy + \int_{up} u\tau_{xy}\, dx - \int_{down} u\tau_{xy}\, dx + \int_{up} v\tau_{yy}\, dx - \int_{down} v\tau_{yy} dx + \int_{right} v\tau_{yx}\, dy - \int_{left} v\tau_{yx}\, dy \quad (3.33)$$

The tensor components have been defined in the previous section in Equation 3.16-18. Using the mean value theorem, the viscous surface integral can be expressed as Equation 3.34.

$$\oiint_s \bar{V}\cdot(\hat{\tau}\cdot d\bar{s}) = (u\tau_{xx})_r^{avg}\Delta y - (u\tau_{xx})_l^{avg}\Delta y + \left(u\tau_{xy}\right)_u^{avg}\Delta y - \left(u\tau_{xy}\right)_d^{avg}\Delta y + \left(v\tau_{yy}\right)_u^{avg}\Delta y - \left(v\tau_{yy}\right)_d^{avg}\Delta y + \left(v\tau_{yx}\right)_r^{avg}\Delta y - \left(v\tau_{yx}\right)_l^{avg}\Delta y \quad (3.34)$$

Equation 3.34 can be expanded to the following form:

$$\begin{aligned}\oiint_s \bar{V}\cdot(\hat{\tau}\cdot d\bar{s}) = &\left[\frac{u_2+u_3}{2}(\tau_{xx})_r - \frac{u_1+u_4}{2}(\tau_{xx})_l\right]\Delta y \\ &+ \left[\frac{u_3+u_4}{2}\left(\tau_{xy}\right)_{\mathrm{u}} - \frac{u_1+u_2}{2}\left(\tau_{xy}\right)_{\mathrm{d}}\right]\Delta x \\ &+ \left[\frac{v_2+v_3}{2}\left(\tau_{yx}\right)_r - \frac{v_1+v_4}{2}\left(\tau_{yx}\right)_l\right]\Delta y \\ &+ \left[\frac{v_3+v_4}{2}\left(\tau_{yy}\right)_{\mathrm{u}} - \frac{v_1+v_2}{2}\left(\tau_{yy}\right)_{\mathrm{d}}\right]\Delta x\end{aligned} \quad (3.35)$$

The heating of the system is represented by the heat addition integral $\oiint_s \bar{q}\cdot d\bar{s}$. The heating of the cell is accomplished via thermal conduction. For thermal conduction heating, Fourier's law can be utilized. Fourier's law states heating due to conduction is proportional to the temperature gradient and cross-sectional area of the direction of heat flow [20]. Mathematically, Fourier's laws can be expressed as:

$$\bar{q} = -k\nabla T = -k\left[\frac{\partial T}{\partial x}\hat{\imath} + \frac{\partial T}{\partial y}\hat{\jmath}\right] \quad (3.36)$$

where k is the thermal conductivity.

The surface integral term for heating, $\oiint_s \bar{q}\cdot d\bar{s}$,can be expanded to Equation 3.37. In the equation, the surface integral was separated based on cell face.

$$\oiint_S \bar{q} \cdot d\bar{s} = \int_{right} qdy - \int_{left} qdy + \int_{up} qdx - \int_{down} qdx \qquad (3.\ 37)$$

With Equation 3.36 and the mean value theorem, the integrals on the right hand side of equation 3.37 can be expressed as:

$$\oiint_S \bar{q} \cdot d\bar{s} = -\left(k\frac{\partial T}{\partial x}\right)_r^{avg} \Delta y + \left(k\frac{\partial T}{\partial x}\right)_l^{avg} \Delta y - \left(k\frac{\partial T}{\partial y}\right)_u^{avg} \Delta x + \left(k\frac{\partial T}{\partial y}\right)_d^{avg} \Delta x \qquad (3.\ 38)$$

In Equation 3.38, the derivative terms can be evaluated in the same manner as the derivatives of the stresses that were expressed in the previous section. Equation 3.20 is a good example of the manner of which a derivative can be resolved. For illustration purposes, the term $\left(k\frac{\partial T}{\partial x}\right)_r^{avg}$ will be evaluated explicitly. The thermal conductivity constant will be expressed as the average of the thermal conductivity constant of nodes for a given face. For the face on the right side of the cell, thermal conductivity coefficient (k) is expressed as:

$$k_r = \frac{(k_2 + k_3)}{2} \qquad (3.\ 39)$$

The derivative $\left(\frac{\partial T}{\partial x}\right)_r$ is approximated by using the nodes neighboring the right cell face. Figure 3.6 can be used as the stencil for derivative approximation. The evaluation results in the following expression:

$$\left(\frac{\partial T}{\partial x}\right)_r = \frac{\left[\frac{1}{2}(T_{3r} + T_{2r}) - \frac{1}{2}(T_3 + T_2)\right]}{\Delta x} \qquad (3.\ 40)$$

The derivative is evaluated by using the forward differencing technique. The derivative approximation is dependent on which face the derivative lies on. The lower face and left face of

the cells use backward differencing techniques while the upper and right face of the cell use forward differencing techniques. Combining Equation 3.39 and 3.40 concludes the evaluation of the term $\left(k\frac{\partial T}{\partial x}\right)_r^{avg}$.

The same way that the term $\left(k\frac{\partial T}{\partial x}\right)_r^{avg}$ is calculated, the rest of the heat conduction terms in Equation 3.38 can be resolved. Thus, resulting in the following expression of the heating term:

$$q_r = -\left(k\frac{\partial T}{\partial x}\right)_r^{avg} = -\frac{(k_2+k_3)}{2}\frac{\left[\frac{1}{2}(T_{3r}+T_{2r})-\frac{1}{2}(T_3+T_2)\right]}{\Delta x} \quad (3.41)$$

$$q_u = -\left(k\frac{\partial T}{\partial y}\right)_u^{avg} = -\frac{(k_4+k_3)}{2}\frac{\left[\frac{1}{2}(T_{3u}+T_{4u})-\frac{1}{2}(T_3+T_4)\right]}{\Delta y} \quad (3.42)$$

$$q_l = -\left(k\frac{\partial T}{\partial x}\right)_l^{avg} = -\frac{(k_1+k_4)}{2}\frac{\left[\frac{1}{2}(T_1+T_4)-\frac{1}{2}(T_{1l}+T_{4l})\right]}{\Delta x} \quad (3.43)$$

$$q_d = -\left(k\frac{\partial T}{\partial y}\right)_d^{avg} = -\frac{(k_1+k_2)}{2}\frac{\left[\frac{1}{2}(T_1+T_2)-\frac{1}{2}(T_{1d}+T_{2d})\right]}{\Delta y} \quad (3.44)$$

Using Equations 3.41-44 and the mean value theorem, the algebraic form of the viscous heating surface integral can be expressed as following:

$$\oiint_s \bar{q}\cdot d\bar{s} = q_r\Delta y - q_l\,\Delta y + q_u\Delta x - q_d\,\Delta x \quad (3.45)$$

Each of the components of the energy equation has now been expressed in its algebraic forms. Using Equation 3.30-32, 3.35, and 3.45, the energy equation (Equation 3.29) can be converted to its algebraic form, Equation 3.46.

$$\left(\frac{d(\rho e)}{dt}\right)_{cell}^{avg}\Delta x\Delta y+\left\{\frac{[(\rho eu)_1+(\rho eu)_4]}{2}-\frac{[(\rho eu)_2+(\rho eu)_3]}{2}\right\}\Delta y$$

$$+\left\{\frac{[(\rho ev)_1+(\rho ev)_2]}{2}-\frac{[(\rho ev)_4+(\rho ev)_3]}{2}\right\}\Delta x$$

$$=-\left\{\frac{[(Pu)_1+(Pu)_4]}{2}-\frac{[(Pu)_2+(Pu)_3]}{2}\right\}\Delta y$$

$$-\left\{\frac{[(Pv)_1+(Pv)_2]}{2}-\frac{[(Pv)_4+(Pv)_3]}{2}\right\}\Delta x$$

$$+\left[\frac{u_2+u_3}{2}(\tau_{xx})_r-\frac{u_1+u_4}{2}(\tau_{xx})_l\right]\Delta y \qquad \textit{(3. 46)}$$

$$+\left[\frac{v_2+v_3}{2}(\tau_{yx})_r-\frac{v_1+v_4}{2}(\tau_{yx})_l\right]\Delta y$$

$$+\left[\frac{u_3+u_4}{2}(\tau_{xy})_u-\frac{u_1+u_2}{2}(\tau_{xy})_d\right]\Delta x$$

$$+\left[\frac{v_3+v_4}{2}(\tau_{yy})_u-\frac{v_1+v_2}{2}(\tau_{yy})_d\right]\Delta x+q_r\Delta y-q_l\,\Delta y+q_u\Delta x$$

$$-q_d\,\Delta x$$

Equation 3.46 is then rearranged such that the time derivative is isolated. This operation results in Equation 3.47. The energy equation is the most complex of the three conservational equations because it is a scalar equation that is influenced by pressure, normal stress , shear stress, and heating.

$$\left(\frac{d(\rho e)}{dt}\right)_{cell}^{avg} = -\frac{\{[(\rho eu)_1 + (\rho eu)_4] - [(\rho eu)_2 + (\rho eu)_3]\}}{2\Delta x}$$

$$-\frac{\{[(\rho ev)_1 + (\rho ev)_2] - [(\rho ev)_4 + (\rho ev)_3]\}}{2\Delta y}$$

$$-\frac{\{[(Pu)_1 + (Pu)_4] - [(Pu)_2 + (Pu)_3]\}}{2\Delta x}$$

$$-\frac{\{[(Pv)_1 + (Pv)_2] - [(Pv)_4 + (Pv)_3]\}}{2\Delta y}$$

$$+\frac{[(u_2 + u_3)(\tau_{xx})_r - (u_1 + u_4)(\tau_{xx})_l]}{2\Delta x} \qquad (3.\ 47)$$

$$+\frac{\left[(v_2 + v_3)(\tau_{yx})_r - (v_1 + v_4)(\tau_{yx})_l\right]}{2\Delta x}$$

$$+\frac{\left[(u_3 + u_4)(\tau_{xy})_u - (u_1 + u_2)(\tau_{xy})_d\right]}{2\Delta y}$$

$$+\frac{\left[(v_3 + v_4)(\tau_{yy})_u - (v_1 + v_2)(\tau_{yy})_d\right]}{2\Delta y} + q_r\frac{1}{\Delta x} - q_l\ \frac{1}{\Delta x} + q_u\frac{1}{\Delta y}$$

$$- q_d\ \frac{1}{\Delta y}$$

Equation 3.6, 3.27, 3.28, and 3.47 are the final algebraic forms of conservational laws that are used by the IDS. To make the scheme more uniform and efficient, the algebraic equations are normalized.

3.2.4 Normalized form of the conservational equations. For algorithm efficiency, it is beneficial to normalize the governing equations. The IDS accomplishes this task by using the freestream values to convert dimensional variables to dimensionless variables. Equation 3.48 displays the equations used to convert the governing equations into dimensionless equations.

$$x_* = \frac{x}{L_{ref}} \quad y_* = \frac{y}{L_{ref}} \quad \rho_* = \frac{\rho}{\rho_\infty} \quad T_* = \frac{T}{T_\infty} \quad a_* = \frac{a}{a_\infty} \quad u_* = \frac{u}{u_\infty} \quad v_* = \frac{v}{u_\infty}$$

$$t_* = \frac{u_\infty t}{L_{ref}} \quad \mu_* = k_* = \frac{\mu}{\mu_\infty} = \frac{k}{k_\infty} \tag{3. 48}$$

In Equation 3.48, the subscript ∞ represents freestream properties. The variable a represents the speed of sound. When the dimensionless variables are incorporated in the governing equations (Equations 3.6, 3.27, 3.28, and 3.47) and the * subscript is left out. Tthe resulting forms become:

1. Dimensionless Mass Equation

$$\left(\frac{\partial(\rho)}{\partial t}\right)_{cell}^{avg} = -\frac{[(\rho u)_1+(\rho u)_4-(\rho u)_2+(\rho u)_3]}{2\Delta x} - \frac{[(\rho v)_1+(\rho v)_4-(\rho v)_2+(\rho v)_3]}{2\Delta y} \tag{3. 49}$$

2. Dimensionless X-momentum Equation

$$\begin{aligned}\left(\frac{\partial(\rho u)}{\partial t}\right)_{cell}^{avg} = &-\frac{\{[(\rho u^2)_1 + (\rho u^2)_4] - [(\rho u^2)_2 + (\rho u^2)_3]\}}{2\Delta x} \\ &- \frac{\{[(\rho uv)_1 + (\rho uv)_4] - [(\rho uv)_2 + (\rho uv)_3]\}}{2\Delta y} \\ &+ \frac{1}{\gamma M_\infty^2}\frac{[((\rho T)_1 + (\rho T)_4) - ((\rho T)_2 + (\rho T)_3)]}{2\Delta x} \\ &+ \frac{1}{Re_{L_{ref}}}\frac{[(\tau_{xx})_r - (\tau_{xx})_l]}{\Delta x} + \frac{1}{Re_{L_{ref}}}\frac{\left[(\tau_{xy})_u - (\tau_{xy})_d\right]}{\Delta y}\end{aligned} \tag{3. 50}$$

3. Dimensionless Y-momentum Equation

$$\left(\frac{\partial(\rho v)}{\partial t}\right)_{cell}^{avg} = -\frac{\{[(\rho v^2)_3 + (\rho v^2)_4] - [(\rho v^2)_2 + (\rho v^2)_1]\}}{2\Delta y} - \frac{\{[(\rho uv)_3 + (\rho uv)_4] - [(\rho uv)_2 + (\rho uv)_1]\}}{2\Delta x} + \frac{1}{\gamma M_\infty^2}\frac{[((\rho T)_1 + (\rho T)_2) - ((\rho T)_4 + (\rho T)_3)]}{2\Delta y} + \frac{1}{Re_{L_{ref}}}\frac{\left[(\tau_{yy})_u - (\tau_{yy})_d\right]}{\Delta y} + \frac{1}{Re_{L_{ref}}}\frac{\left[(\tau_{yx})_r - (\tau_{yx})_l\right]}{\Delta x} \quad (3.51)$$

4. Dimensionless Energy Equation

$$\left(\frac{d(\rho e)}{dt}\right)_{cell}^{avg} = -\frac{\{[(\rho eu)_1 + (\rho eu)_4] - [(\rho eu)_2 + (\rho eu)_3]\}}{2\Delta x}$$
$$-\frac{\{[(\rho ev)_1 + (\rho ev)_2] - [(\rho ev)_4 + (\rho ev)_3]\}}{2\Delta y}$$
$$-\frac{1}{\gamma M_\infty^2}\frac{\{[(\rho Tu)_1 + (\rho Tu)_4] - [(\rho Tu)_2 + (\rho Tu)_3]\}}{2\Delta x}$$
$$-\frac{1}{\gamma M_\infty^2}\frac{\{[(\rho Tv)_1 + (\rho Tv)_2] - [(\rho Tv)_4 + (\rho Tv)_3]\}}{2\Delta y}$$
$$+\frac{1}{Re_{L_{ref}}}\frac{[(u_2 + u_3)(\tau_{xx})_r - (u_1 + u_4)(\tau_{xx})_l]}{2\Delta x} \qquad (3.\ 52)$$
$$+\frac{1}{Re_{L_{ref}}}\frac{\left[(v_2 + v_3)(\tau_{yx})_r - (v_1 + v_4)(\tau_{yx})_l\right]}{2\Delta x}$$
$$+\frac{1}{Re_{L_{ref}}}\frac{\left[(u_3 + u_4)(\tau_{xy})_u - (u_1 + u_2)(\tau_{xy})_d\right]}{2\Delta y}$$
$$+\frac{1}{Re_{L_{ref}}}\frac{\left[(v_3 + v_4)(\tau_{yy})_u - (v_1 + v_2)(\tau_{yy})_d\right]}{2\Delta y}$$
$$+\frac{1}{Re_{L_{ref}} Pr\, M_\infty^2}\left\{q_r\frac{1}{\Delta x} - q_l\frac{1}{\Delta x} + q_u\frac{1}{\Delta y} - q_d\frac{1}{\Delta y}\right\}$$

In the new, dimensionless equations, there are several new variables that have been introduced. These variables are the Reynolds number ($Re_{L_{ref}}$), Mach number (M_∞), Prandtl number (Pr), and ratio of specific heats (γ), which are defined in equation 3.53-56

$$Re_{L_{ref}} = -\frac{\rho_\infty u_\infty L_{ref}}{\mu_\infty} \tag{3. 53}$$

$$M_\infty = -\frac{u_\infty}{a_\infty} \tag{3. 54}$$

$$Pr = \frac{\mu_\infty C_p}{k} \tag{3. 55}$$

$$\gamma = \frac{C_p}{C_v} \tag{3. 56}$$

Additionally in the dimensionless forms of the governing equations, the pressure and specific energy are transformed to the following forms:

$$P = \frac{\rho T}{\gamma M_\infty^2} \tag{3. 57}$$

$$e = \frac{T}{\gamma(\gamma - 1)\gamma M_\infty^2} + \frac{u^2 + v^2 + w^2}{2} \tag{3. 58}$$

The dimensionless forms of the governing equations are the final forms that are utilized by the IDS. Equations 3.49-52 provide the time derivative of the conserved variables. These derivatives provide important information that will be used to march the solution forward in time. The time derivatives, however, are only valid at the center of the cell, which corresponds to an imaginary node. The next section will explicitly discuss how the temporal fluxes are used to march the solution forward in time.

3.3 The IDS Time Marching Methods

So far, the governing equations and the ability to extract the temporal flux of the conserved variables is not unique compared to other numerical schemes. The uniqueness of the IDS comes in the manner in which the scheme marches the solution forward in time. From the previous section, the governing equations provide four equations with four unknown variables $(\rho, \rho u, \rho v, e)$. This closed system of equations can be solved. For mathematical convenience, the unknown variables are processed in a solution vector U_m.

$$U_m = \begin{bmatrix} U_{m1} \\ U_{m2} \\ U_{m3} \\ U_{m4} \end{bmatrix} = \begin{bmatrix} \rho_m \\ (\rho u)_m \\ (\rho v)_m \\ e_m \end{bmatrix} \tag{3. 59}$$

The subscript m represents the mean value, which is uniquely calculated in the IDS. Starting from a given time (t), the solution vector U_m can be updated to obtain the new solution vector at time $t + \Delta t$. This can be accomplished by using an explicit time marching scheme. In the case of IDS, the first order Taylor series expansion is used to obtain the following marching scheme:

$$(U_m)_{i,j}^{t+\Delta t} = (U_m)_{i,j}^{t} + \left(\frac{\partial U_m}{\partial t}\right)_{i,j} \Delta t \tag{3. 60}$$

The innovation of the IDS is revealed in how the right hand side of Equation 3.60 is handled. The solution vector $(U_m)_{i,j}^{t}$ is evaluated as the average of the cells and nodes in a control volume. Let the generic function U represent the un- manipulated conserved variables:

$$U = \begin{bmatrix} \rho \\ \rho u \\ \rho v \\ e \end{bmatrix} \tag{3. 61}$$

The first step in the calculation of the solution vector is to calculate the center value of all the individual spatial cells (a,b,c,d) within a control volume. Refer to Figure 3.2 for a diagram of the cell and control volume. The value of the center of any spatial cell is the arithmetic average of all the node values in that given cell. The following equation is the average U value at the center of a given spatial cell (a, b, c, or d).

$$U_{cell}^{avg} = \frac{U_1 + U_2 + U_3 + U_4}{4} \tag{3. 62}$$

The final step is to calculate U at the center of the control volume. U at the center of the control volume is the arithmetic average of the center values of the four spatial cells within the control volume. Equation 3.63 displays the U value for a given control volume.

$$(U_m)_{i,j}^{t} = U_{i,j}^{avg} = \frac{U_a^{avg} + U_b^{avg} + U_c^{avg} + U_d^{avg}}{4} \tag{3. 63}$$

The temporal flux vector $\left(\frac{\partial U_m}{\partial \mathrm{t}}\right)_{\mathrm{i,j,k}}$ is obtained in a similar manner to solution vector U_m. However, the temporal flux vector utilizes the temporal cell for a given control volume. For assistance refer to Figure 3.3. The first step is to obtain the temporal vertices of the temporal cells. The vertices of the temporal cell are obtained by using the dimensionless algebraic forms of the governing equations (Equations 3.49-52) to retrieve the time rate derivative of the conserved variables. The governing equations are applied to the four spatial cells within a control volume. The final step is to obtain the time derivative at the center of the temporal cell. This is accomplished by taking the average of the time derivatives at the imaginary nodes/vertices of the temporal cell within the control volume.

$$\left(\frac{\partial U_m}{\partial t}\right)_{i,j} = \left(\frac{\partial U_m}{\partial t}\right)_{i,j}^{avg} = \frac{\frac{\partial U}{\partial t}_a + \frac{\partial U}{\partial t}_b + \frac{\partial U}{\partial t}_c + \frac{\partial U}{\partial t}_d}{4} \tag{3. 64}$$

When calculating the time step size (Δt), it is important not to take a step that is too large. If the step size is too large the solution will oscillate or even diverge. For insurance of scheme stability, the time steps are calculated based on the Courant-Friedrichs-Lewy (CFL) defined by the following source [7]. This results in the following equation:

$$\Delta t = C\left[\frac{|u_{i,j}|}{\Delta x} + \frac{|v_{i,j}|}{\Delta x} + a_{i,j}\sqrt{\frac{1}{\Delta x^2} + \frac{1}{\Delta y^2}} + \frac{2}{Re_{L_{ref}}} max\left(\frac{{}^{4}/_{3}, \left({}^{\gamma\mu_{i,j}}/_{Pr}\right)}{\rho_{i,j}}\right)\left(\frac{1}{\Delta x^2} + \frac{1}{\Delta y^2}\right)\right]^{-1} \tag{3. 65}$$

In Equation 3.65, the symbol C is the Courant number, which is between 0.5 and 0.8. Each node has its own time step size; however, only the smallest time step is used in the marching process.

At this point, all of the terms of the left hand side of equation 3.60 are known. This allows one to update the solution and march the solution vector forward in time. Once the new conserved variables are obtained, it is important to decouple the conserved variables to their primitive variables. The primitive variables are used to calculate the terms in the governing equations such as friction stress tensor and heat rates. The following equations are used to decouple the primitive variables:

$$\rho_{i,j}^{t+\Delta t} = (U_{m1})_{i,j}^{t+\Delta t} \tag{3. 66}$$

$$u_{i,j}^{t+\Delta t} = \frac{(U_{m2})_{i,j}^{t+\Delta t}}{(U_{m1})_{i,j}^{t+\Delta t}} \tag{3. 67}$$

$$v_{i,j}^{t+\Delta t} = \frac{(U_{m3})_{i,j}^{t+\Delta t}}{(U_{m1})_{i,j}^{t+\Delta t}} \tag{3. 68}$$

$$T_{i,j}^{t+\Delta t} = \left[\frac{(U_{m4})_{i,j}^{t+\Delta t}}{(U_{m1})_{i,j}^{t+\Delta t}} - \frac{u_{i,j}^{t+\Delta t} + v_{i,j}^{t+\Delta t}}{2}\right]\gamma(\gamma - 1)M_{\infty}^{2} \tag{3. 69}$$

With the updated primitive variables, the whole cycle can be repeated again to move forward in time. This is accomplished by replacing the old primitive variables with the newly acquired primitive variables. The solution is marched forward in time until the solution is converged or once one has reached a satisfied end point.

CHAPTER 4

Results and Discussion

Detailed in this Chapter, Chapter 4, are the results of applying the IDS to two supersonic fluid dynamic problems which are known to lend themselves to non-rectangular flow field domains containing complex interactions. These two supersonic fluid dynamic problems were chosen because they are supported by credible experiment measurements and observations. In this analysis, the IDS formulation was implemented through a FORTRAN code, and its numerical outcomes were analyzed through the use of TECPLOT 360 The IDS code, which was developed in by Dr. Elamin [6], was modified with the initial and boundary conditions appropriate for the two problems of interest. It is of interest to note that no changes were made to the initial IDS formulations, no parameters were tweaked and no assumptions relative to the problems were made. However, great efforts were made to closely match the boundary conditions that are pertinent to the simulation of each problem. The two supersonic experiments that were chosen for validation are

(a) the supersonic flow over a rearward facing step problem, refer to section 4.1.

(b) the supersonic flow over an open cavity problem, refer to section 4.2.

In order to validate the IDS, the results obtained from (a) and (b) are compared to the experimental data [2122].Detailed descriptions of this validation process are documented in Sections 4.1 and 4.2, respectively. In addition, in each case, the technical format use to describe the validation process is as follows:

1. A discussion of the problem physics
2. A discussion of the boundary and initial conditions set up
3. A discussion and comparison of the results with the experimental data

4.1 Supersonic Flow over Rearward-Facing Step (RFS) Problem

The first problem that will be tackled is the supersonic flow over a rearward-facing step (RFS) problem. The RFS problem is a great benchmark problem that is used to validate CFD codes. It exhibits various complex flow phenomena, including boundary layer separations, boundary layer reattachment, expansion waves, and shock wave/boundary layer interaction [21]. Several researchers have conducted experimental studies of RFS problems. To reference a few: J. McDaniel et al. [21], Chen Zhi et al. [23], R. Leonard and N. Chokani [24], and P. Oshkai et al. [25]. In additional to experimental research, several researchers investigated the rearward step problem via CFD investigation. These researchers include: D. R. Eklund et al. [26], H Liu et al. [27], A. Karimi et al. [28], A. S. Yang, et al. [29], and R. Lohner et al. [30]. These research efforts have introduced and described several of the physical phenomena that can be expected for this problem.

There are several interesting physical features that are associated with supersonic flow over a rearward facing steps. The complexity of the problem makes it a great problem to validate numerical schemes. Figure 4.1 displays a diagram with the flow field features that are expected to be observed.

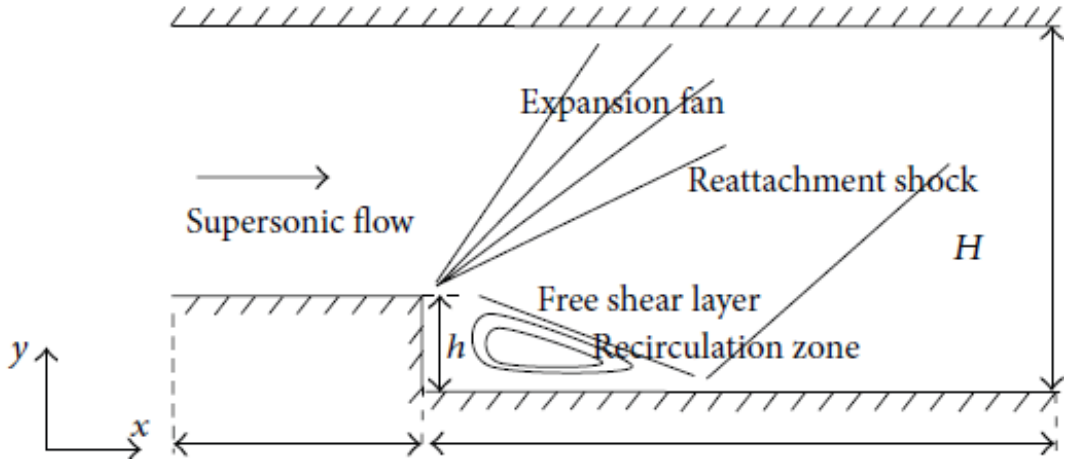

Figure 4.1. Diagram of RFS flow field features [27].

Looking at Figure 4.1, when the flow reaches the sharp turn, the flow will expand. This expansion is indicated by the expansion fan. The expansion fan is a major feature that is expected to be observed clearly in the numerical solution. Close to the base of the step, there will be a recirculation region. The recirculation region is caused by the fact that the fluid close to the walls (step surface and bottom of step surface) is moving slow while the fluid way from the wall is moving fast. This discrepancy in flow speeds causes the fluid trapped in between the fast moving fluid and slow moving fluid to recirculate. At the end of the free shear layer, the reattachment shock begins. The reattachment shock forces the flow downstream of the shock to move parallel to the floor surface. The expansion fan, recirculation region, and reattachment shock are the three main features that will be expected in the computational results.

4.1.1 RFS problem setup. The rearward step problem geometry and flow field parameters were taken from a conference paper by J. McDaniel et al. [21]. Figure 4.2 displays the geometry that is simulated in the IDS code. The flow is traveling from the left boundary (inflow) to the right boundary (outflow). The outflow location was set significantly far from the area of interest to avoid interfaces between outflow boundary condition and the domain solution.

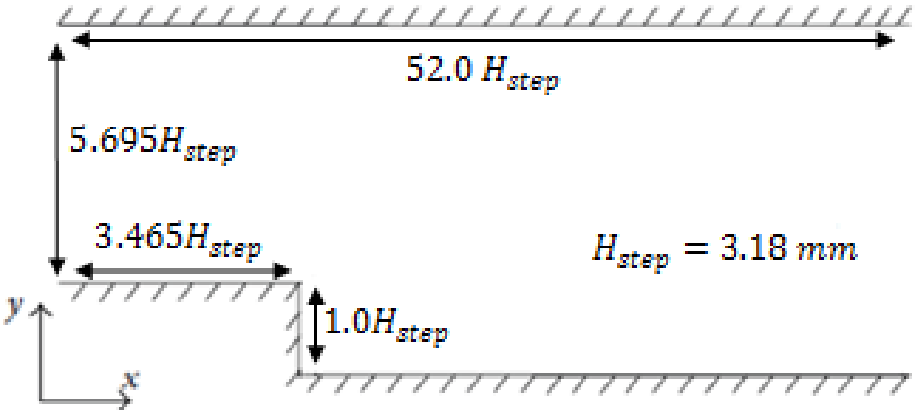

Figure 4.2. Computational RFS geometry [27].

4.1.2 RFS problem boundary and initial conditions. The flow conditions are described by the experimental setup. All these parameters are summarized in Table 4.1. To achieve the flow conditions listed Table 4.1, the air supply for the wind tunnel used a centrifugal air compressor and a high pressure storage volume. Table 4.1 provides all of the essential parameters. The rest of the missing parameters such as velocity, density, and speed of sound were calculated using the data on the table.

Table 4.1

Rearward-facing step problem Parameters

Parameter	Freestream Condition
Mach at Freestream	2.0
Pressure at Freestream	35 KPa
Temperature at Freestream	167K
Dynamic viscosity at Freestream	$1.135 \times 10^{-5} - 005\ \frac{J}{m \cdot s}$
Gas constant	$287.0\ \frac{J}{Kg \cdot K}$
Ratio of specific heats	1.4

The creation of the computational domain was introduced in Chapter 3. The RFS domain is a multi-block grid. The RFS domain has an L-shape that is turned 180°. A sketch of the computational domain is shown in Figure 4.3.

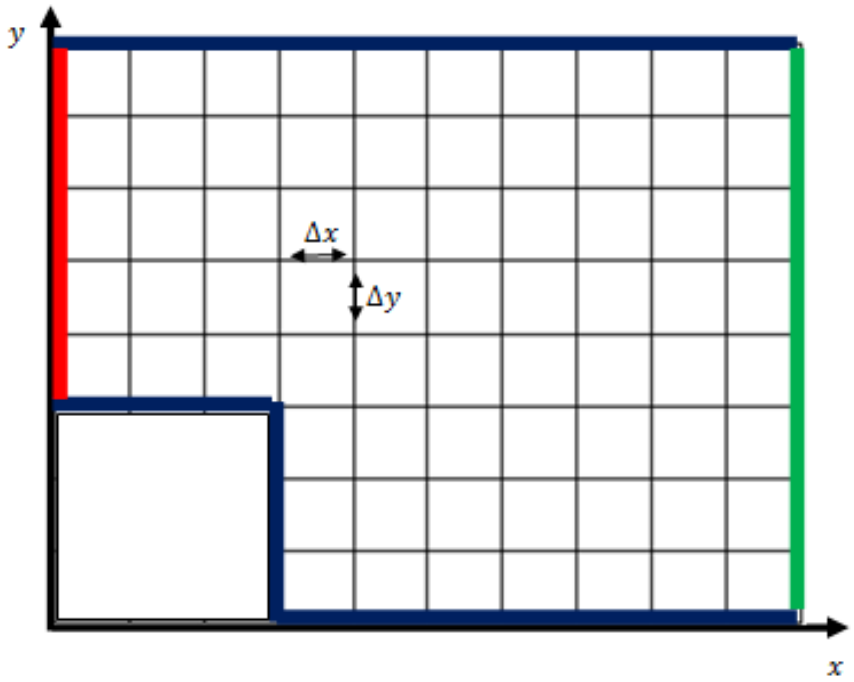

Figure 4.3. RFS computational domain with colored boundaries.

Surrounding the computational domain are the boundaries. The boundaries in Figure 4.3 are colored coded for convenience. The red colored boundary is the inlet boundary. This boundary has all of the primitive variable specified based on the information on Table 4.1. The blue boundary is the solid surface boundary. The solid surface boundary has a no slip condition i.e. zero velocity vector. Additionally, the boundary is assumed to be insulated and has zero pressure gradient on the surface. The last boundary, that is colored green, is the outflow boundary. This boundary has the primitive variables extrapolated from the domain nodes. The extrapolation is set such that the node next to the boundary is the average of the neighboring two nodes. From that condition, the boundary node can be set to be a function of the next two inner nodes. Table 4.2 displays some of the boundary conditions and their specific equations. On the table, the surface boundary is applicable to the top surface. Furthermore, the subscripts i_{max} and j_{max} represent the total number of nodes in the x-direction and in the y-direction , respectively.

Table 4.2

RFS Boundary Conditions

Parameter	Inlet BC	Outlet BC	Surface BC
U-velocity	$(u_*)_{1,j} = 1$	$(u_*)_{imax,j} = 2.0(u_*)_{imax-1,j} - (u_*)_{imax-2,j}$	$(u_*)_{1,j} = 0$
V-velocity	$(v_*)_{1,j} = 0$	$(v_*)_{imax,j} = 2.0(v_*)_{imax-1,j} - (v_*)_{imax-2,j}$	$(v_*)_{1,j} = 0$
Temperature	$(T_*)_{1,j} = 1$	$(T_*)_{imax,j} = 2.0(T_*)_{imax-1,j} - (T_*)_{imax-2,j}$	$(T_*)_{i,jmax} = (T_*)_{i,jmax-1}$
Density	$(\rho_*)_{1,j} = 1$	$(\rho_*)_{imax,j} = 2.0(\rho_*)_{imax-1,j} - (\rho_*)_{imax-2,j}$	$(\rho_*)_{i,jmax} = \frac{(T_*)_{i,jmax-1}(\rho_*)_{i,jmax-1}}{(T_*)_{i,jmax}}$

Along with the boundary conditions, initial flow field information is needed before the IDS can be applied. For the problem at hand, the initial condition was set to be the same as the inlet boundary condition. This means, all of the nodes within the boundary condition had the same aerodynamic properties as that listed on the Inlet BC column on Table 4.2.

4.1.3 RFS problem results. Using the geometry, domain, initial condition and the boundary condition information, the IDS can be implemented to march the initial condition forward in time. The solution is explicitly marched until the exit condition or the steady state condition is reached. In this investigation, steady state condition was considered to be reached when the maximum residual of the mass, momentum, and the energy fluxes at each internal grid

point varied less than 1.0×10^{-5}. The residual was defined as the difference between the new and the old value of the flux for each two consecutive time steps.

The first study that was conducted was a solution convergence study. The rearward grid problem was solved for three different grid densities, $501 \times 501, 1001 \times 1001,$ and 2001×2001. Figure 4.4 display the residual studies. In the figure, the error is decreasing in a consistent manner as iterations increase. This steady decrease illustrates that the time steps are small enough for the scheme to be stable.

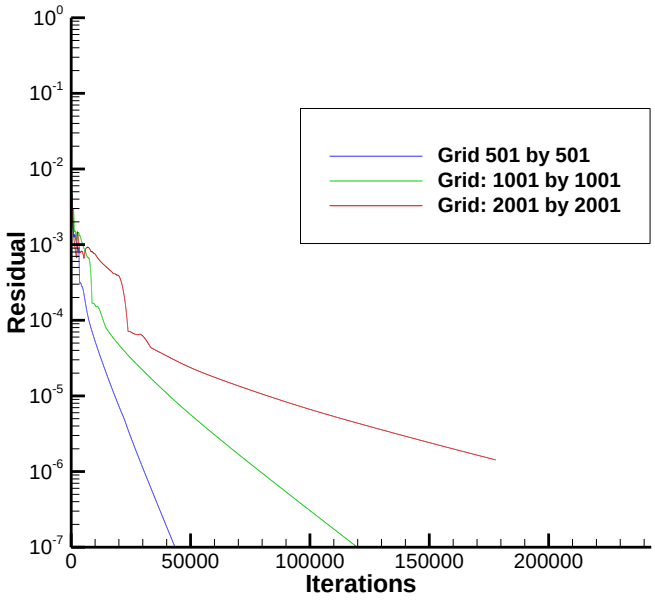

Figure 4.4. Solution convergence study.

The 501×501 and 1001×1001 grid system ran until they reached a residual of less than 1.0×10^{-10}. The time to run the 2001×2001 grid system took a longer time. After its termination, the residual had reached 1.43×10^{-6}. Clearly, each of the solution can be assumed to have reached its steady state.

A grid convergence study was also conducted for the RFS problem. The pressure, temperature, and velocity vectors profiles were plotted at $x = 5.221H_{step}$. These profiles are

displayed in Figure 4.5. All of the profiles in Figure 4.5 show the same trend; indicating, qualitatively, the results are favorable. Based on the profiles, the IDS is able to perform well even for course grids. On further examinations, the grids seem to have converged for the velocity and temperature profiles. The pressure profile, on the other hand, shows that the grids have not completely converged. The pressure profile also indicates that the pressure is more grid sensitive compared to the other variables.

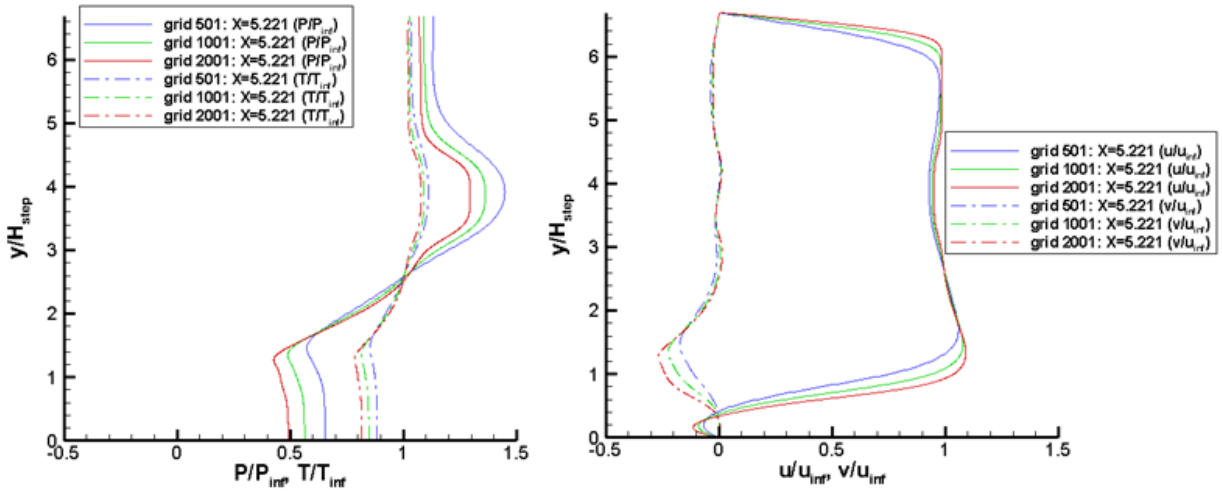

Figure 4.5. Grid convergence study.

The 1001×1001 grid seems to be the optimal grid system to use because its solution converged at a reasonable rate based on the solution convergence study, Figure 4.4. Additionally, the discrepancy between the very fine grid (2001×2001) and fine grid (1001×1001) seems to be reasonably small. From this point forward, the fine grid will be used for experimental comparisons.

The computational data that were obtained will now be compared to the experimental results. Figure 4.6 exhibits the pressure contour plot obtained by the IDS code. For comparison,

Figure 4.7 displays a pressure contour plot obtained by Planar Laser-Induced Iodine Fluorescence (PLIIF) technique.

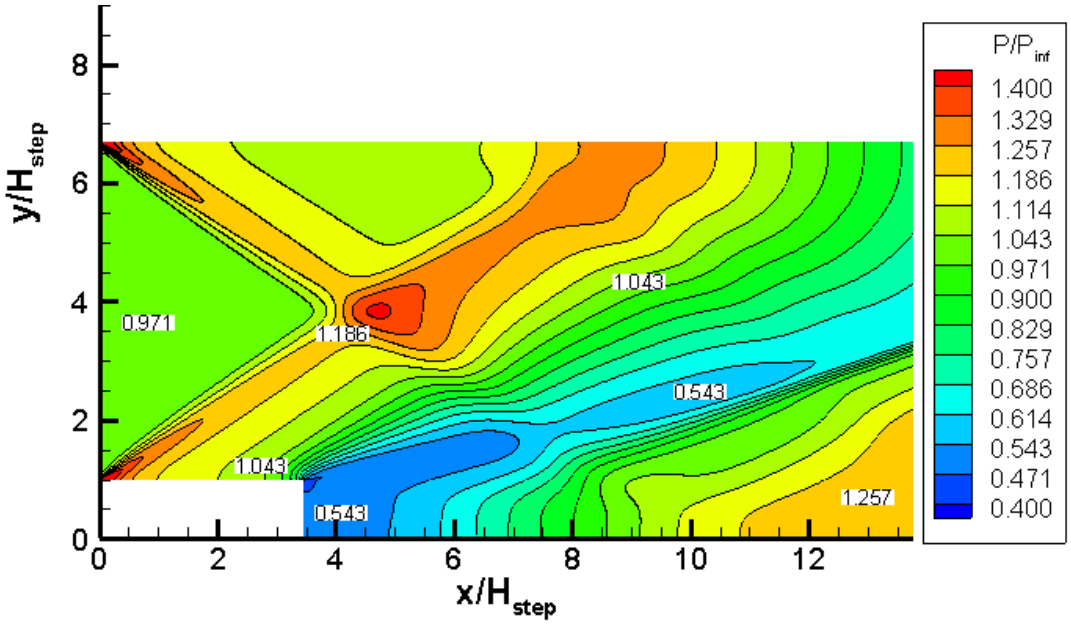

Figure 4.6. The IDS pressure contour plot.

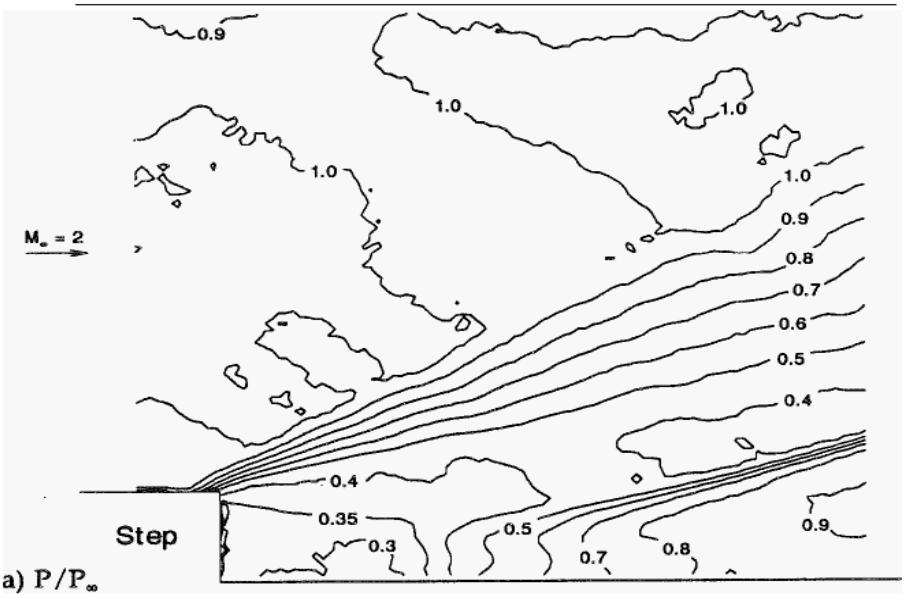

Figure 4.7. The PLIIF pressure contour plot [21].

Qualitatively, the two figures look very similar except for one significant difference. The IDS pressure contour plots exhibits two oblique shocks that originate from the inlet and surface boundary intersections. These two oblique shocks are identified by the rapid increase in pressure. The two oblique shocks collide with each other a short distance upstream of the edge of the step. The two shocks act like "leading edge shocks". These leading edge shocks are present in the solution because the incoming supersonic flow experiences a sudden halt due to the no slip condition. To accommodate for the sudden changes, the compression waves appear. The experimental contour plot, on the other hand, does not exhibit these two oblique shocks. This is because the flow in the experiment is already developed by the time it reaches the test section. The ability to capture these leading edge shocks is not a faulty in the IDS rather it is a failure to use the correct boundary conditions that simulate the experiment's conditions.

The presences of these leading edge shocks cause the discrepancy between the IDS and experimental results. As a matter of fact, the rise in pressure due to the shocks has caused a shift in pressure throughout the whole computational domain. This shift in pressure is noticed since the experimental pressure field is lower than the IDS pressure field. After the two leading edge shocks collide, the shock that originated from the lower surface diffracts on ward until it hits the top surface. The upper shock does seem to have a diffracted portion. The trend of the contour lines indicates that the diffracted portion of the upper shock is diminished due to the presence of an expansion fan.

Even though the two shocks interfere with the quantitative information, the qualitative results are in good agreement with the experimental results. Both contour plots display a clear expansion fan region. This expansion fan is recognized by the smooth pressure decrease that is centered at the edge of the step. Furthermore, both of the contour plots display the reattachment

shock. The reattachment shock is located after the expansion fan. There is a space of nearly constant pressure between the end of the expansion fan and the start of the reattachment shock. The reattachment shock is identified by the rapid increase in pressure. It is also noteworthy to observe that the reattachment shock does not hit the bottom surface. Instead, the reattachment shock is dissolved or horizontally stretched as it gets close to the surface. Both contour plots are able to capture this feature.

Figure 4.8 displays the IDS temperature contour plots. The temperature contour plot looks very similar to the temperature contour plot.

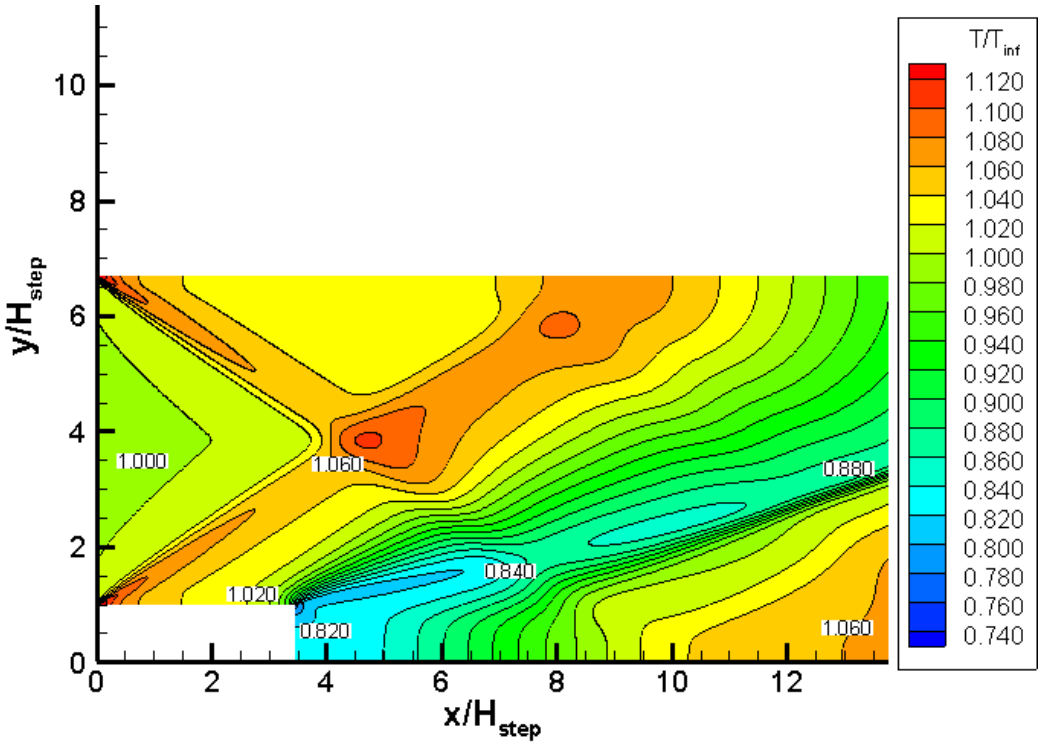

Figure 4.8. The IDS pressure contour plot.

The presence of the leading edge shocks can be faintly observed in Figure 4.8. The low temperature gradient at the inlet indicates that the leading edge shocks do not influence the temperature contours as much as they do with the pressure contours. Nevertheless, the shocks have influence in certain areas. For example, the top surface (roof) has a region of high

temperature. This localized high temperature zone is located at the same position where the diffracted leading edge shock hits. Needless to say, this has caused a disagreement between the IDS and experimental temperature contour plots.

Figure 4.9 display the PLIIF temperature contour plot from the experiment. The Figure 4.9 is the corresponding experimental contour plot of Figure 4.8.

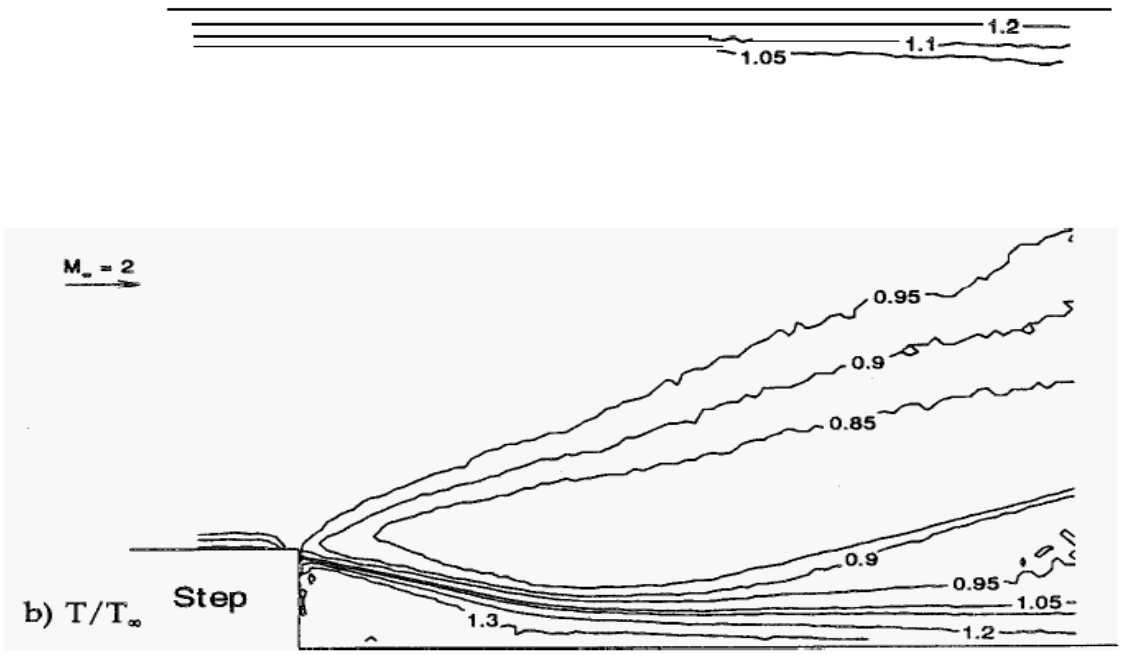

Figure 4.9. The PLIIF temperature contour plot [21].

Looking at both Figure 4.8 and 4.9, it is clear that the expansion fan and reattachment shock are seen in both temperature contour plots. However, the contour lines at the bottom of the step in Figure 4.8 are different from the contour lines at the bottom surface of Figure 4.9. These contour lines on Figure 4.8 indicate the temperature at the surface has a low gradient in the vertical direction. Conversely, the experimental temperature distribution toward the bottom surface has non-zero gradient in the vertical direction. This disagreement between the numerical and experimental trend could be as a result of the insulated boundary condition used by the IDS.

Next to the step is a region of recirculation. This phenomenon was captured by the IDS results as shown in Figure 4.10. Figure 4.10 exhibits a Mach number contour plot with streamlines superimposed on it. The streamlines clearly indicate the region of flow circulation.

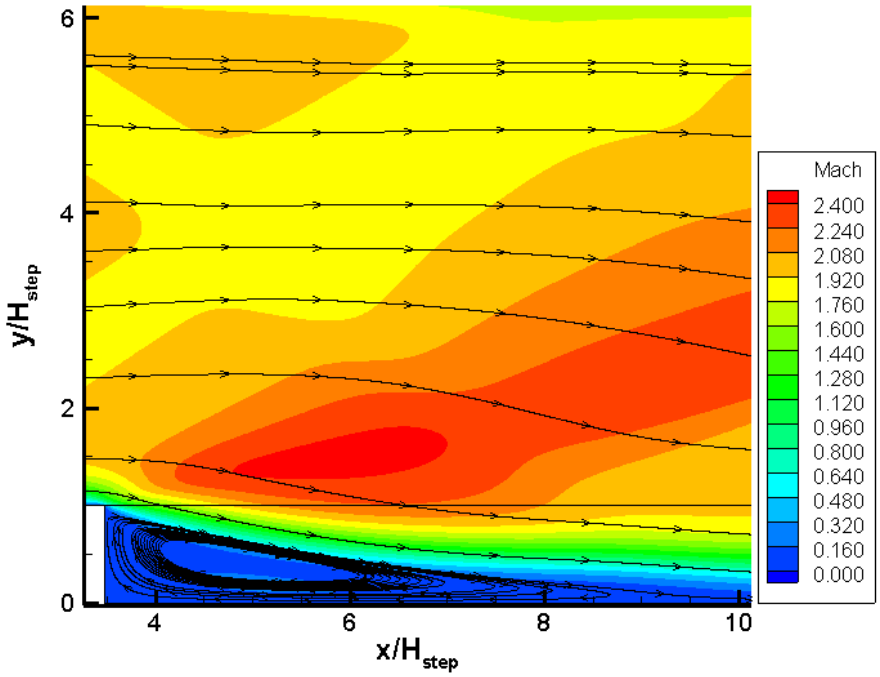

Figure 4.10. Mach number contour plot with streamlines.

From Figure 4.10, the expansion fan is identified by the region of Mach number increase. The region between the recirculation and expansion fan marks the shear layer. The shear layer is identified by the region where there is a sharp mach gradient. Note that in the subsonic regions, there is no Mach number increase because an expansion fan is a supersonic flow phenomenon. The effects on subsonic regions are more clearly observed for a zoomed out view of Figure 4.10. Figure 4.11 displays the Mach number contour plot for the whole domain. As indicated by the streamlines in Figure 4.11, the flow starts off parallel to the walls. At the edge of the step, the flow is turned due to the expansion fan. At the end of the fan the flow is turned to be parallel

with the walls. This second turn is caused by the reattachment shock. Notice that in the areas where the flow is subsonic, compression and expansion waves are not present.

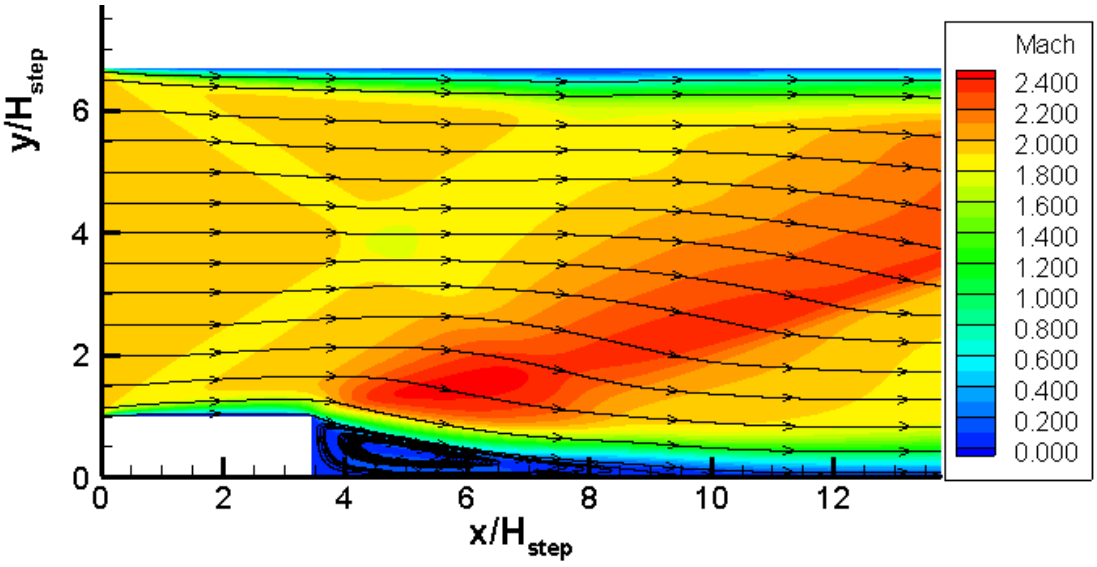

Figure 4.11. Mach number contour plot with streamlines (whole domain).

The contour plots tend to only give qualitative information. It is difficult to compare the numerical and experimental results using just contour plots. For a more quantitative comparison, line plots have be used. Y-axis vs. temperature, pressure, and velocity plots have been taken at $x = 2.465H_{step}, 3.388H_{step}, 5.2208H_{step}, 6.465H_{step},\ and\ 10.155H_{step}$. These locations capture the inlet, reward step, flow circulation, and shock reattachment regions. To obtain the aerodynamic properties, McDaniel et al used varies measurement instruments, which include: Laser-Induced-Iodine Fluorescence (LIIF), Planar Laser-Induced Iodine Fluorescence (PLIIF), and Laser Doppler Anemometry (LDA).

Starting off, the profiles at the inlet are displayed in Figure 4.12. In the IDS pressure profile shown in Figure 4.12, there is a clear jump in pressure in the region close to the walls. This pressure jump is due to the leading edge shocks. As it was mentioned earlier, the shock disturbances deviate the numerical solution from the experimental data. Towards the middle of

the channel, the shock interference is not felt; thus, there is a stronger agreement between the numerical and experimental solution.

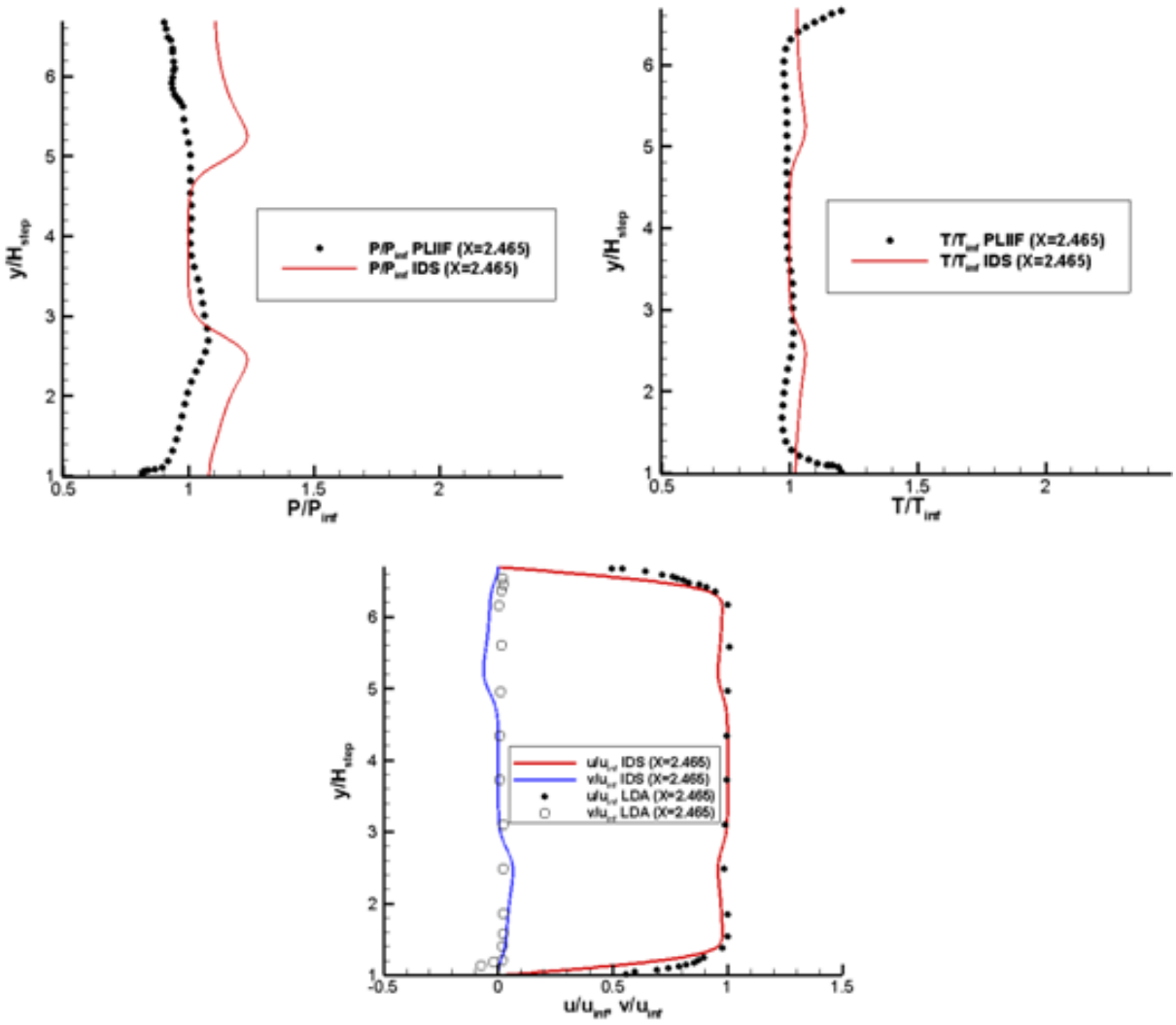

Figure 4.12. Comparison of IDS and experimental profiles at $x = 2.465H_{step}$.

In the temperature contour plot, the leading edge shocks had weak influence on the temperature distribution. This observation is confirmed with the temperature profile in Figure 4.12. The numerical and experimental temperature plots resemble each other well. Close to the walls, there is still a small temperature jump due to the presence of the shocks. The velocity profiles are in good agreements as well. The boundary layer is captured by the scheme. The

boundary layer can be seen in the u-velocity profile. Close to the wall there is a high u-velocity gradient due to the dominance of viscous forces. In regions close to the surface (around $0.12H_{step}$) the laser measurement systems have systematic errors due to wall light scattering [21]. In these regions the experimental data should be disregarded. Therefore, the discrepancy between the experimental and numerical can be attributed to experimental uncertainties. Like the temperature profile, there is a small u and v velocity alterations in the location where the shocks are present; however, the velocity alteration are faint.

The next profiles are taken just upstream of the step at $x = 3.388H_{step}$. Figure 4.13 displays these profiles. The pressure profile obtained by the IDS has a higher pressure compared the experimental profile. Once again this feature is due to the leading edge shocks. Towards the edge of the step, the experimental and numerical pressure distributions are more similar. This could be due to the fact that the expansion processes is beginning to take place. The expansion fan lowers the high pressure that was caused by the leading edge shocks. Compared to the boundary layer pressure profile in Figure 4.12, the boundary layer pressure profile of Figure 4.13 is less. This further supports the idea that the expansion fan is taking place.

In the temperature and velocity profiles of Figure 4.13, the numerical and experimental data are in good agreements. This is expected since the leading edge shocks did not affect temperature and velocity so much. In the boundary close to the step, the temperature seems to decrease; while the v-velocity in the boundary is negative. These trends are mostly caused by the expansion.

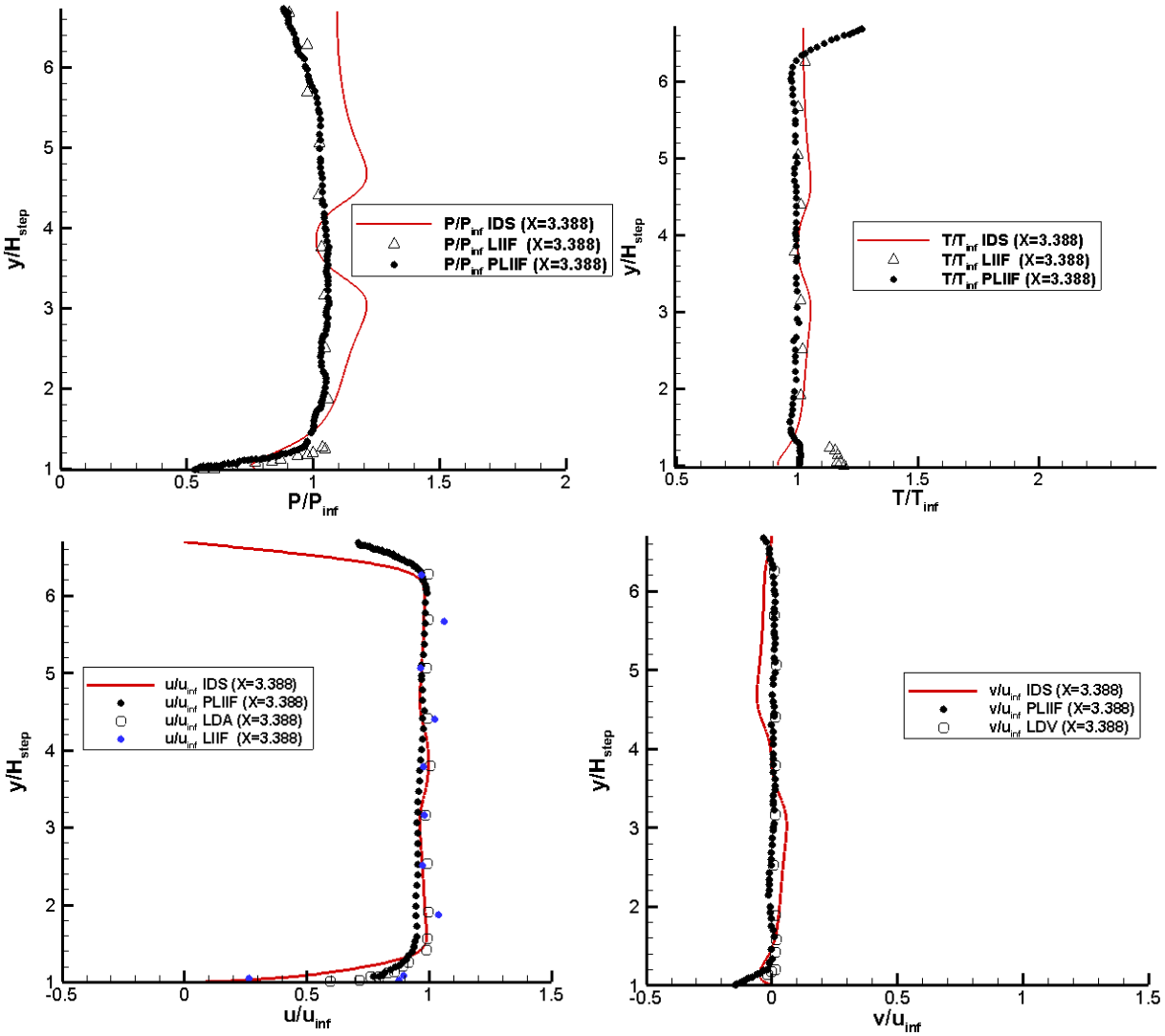

Figure 4.13. Comparison of IDS and experimental profiles at $x = 3.388H_{step}$.

Figure 4.14-16 display the profiles along the floor of the step. Out of the three measured primitive variable profiles, pressure distribution has the largest discrepancy. The numerical and experimental data only match in a few locations. The discrepancies are generally in the regions above the leading shock intersections and the regions close to the surface. At this point, it is evident that the leading edge shocks have disturbed the pressure throughout the domain. The IDS results generally have higher pressure. This effect is most prevalent in regions downstream of the intersection of the two leading edge shock.

The pressure profile at $x = 5.2208H_{step}$ and $x = 6.465H_{step}$ are similar. This could be because both profiles pass through the recirculation region and expansion fan. According to the Mach contour plot, the recirculation region seems to end close to $x = 9H_{step}$. The pressure profile in Figure 4.14 ($x = 5.2208H_{step}$) displays the large pressure jump in the region between $y = 3H_{step}$ to y= $5H_{step}$. This section corresponds to the location of the shock intersection point. The same observation can be made for the pressure profile in Figure 4.15. In Figure 4.14, the region $y = 1H_{step}$ to $y = 3H_{step}$ is the expansion fan location. In this area, the experiment and numerical results are in good agreement. The region below $y = 1H_{step}$ is the recirculation region. Note that in this region the pressure profile deviates from the experiment results. This deviation can be caused by ill applied boundary condition.

The temperature profiles and pressure profiles at $x = 5.2208H_{step}$ and $x = 6.465H_{step}$ display the same behaviors. The temperature profiles have better agreements between the experimental and numerical results; however, in regions close to the bottom surface, the experimental and numerical data diverge from each other.

The velocity profiles, especially the v-velocity profiles, in Figure 4.14-15 match with the experimental profiles fairly well. In the regions close to the surface, the u-velocity results and experimental results diverge from each other. The difference between the experimental and numerical u-velocity profile is mainly due to systematic errors. The experimental u-velocity profiles do not seem to uphold the no-slip condition. It is therefore difficult to discern the errors of the IDS results close to the surface because the experiment's velocity measurements have some inherent errors.

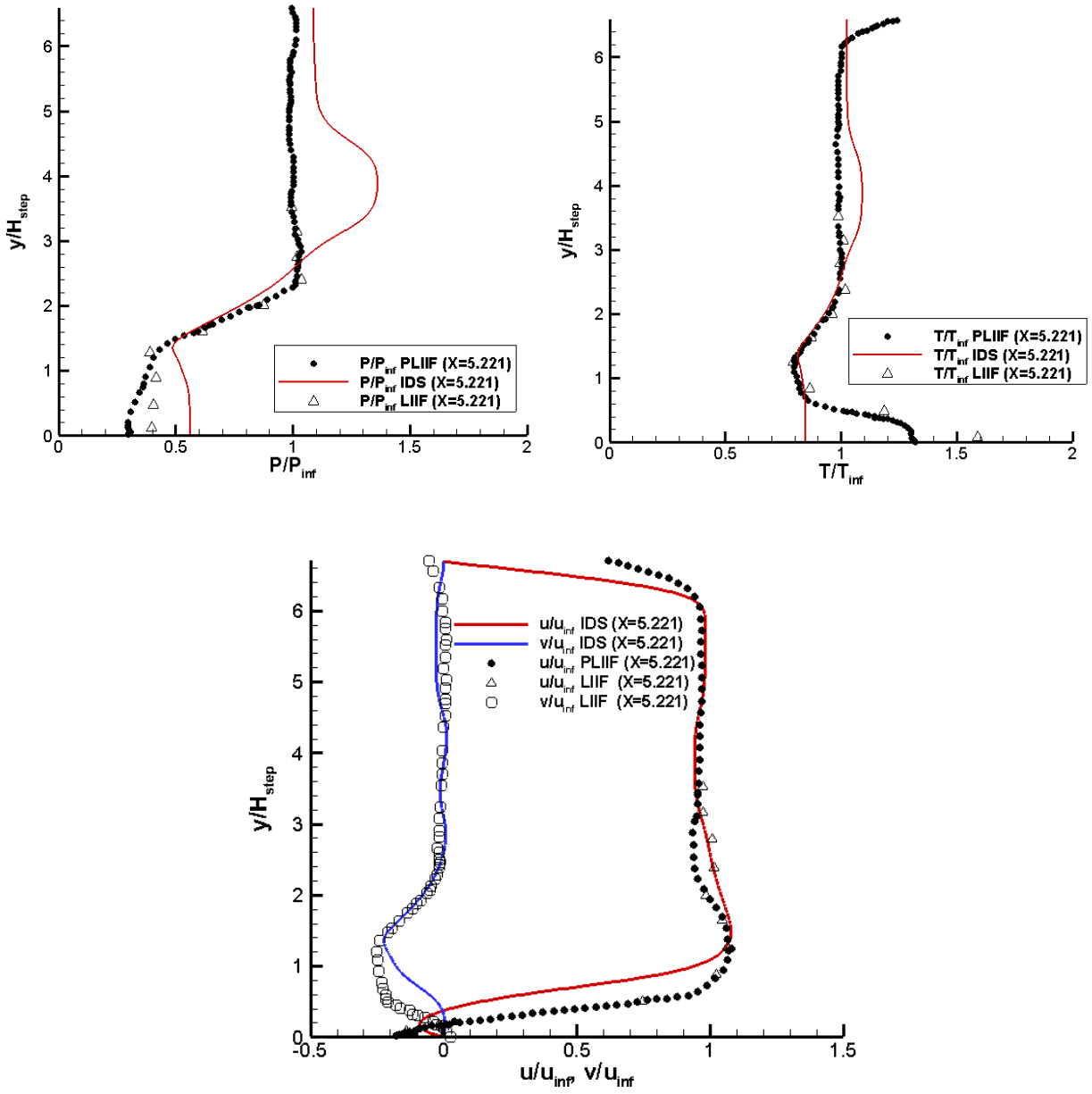

Figure 4.14. Comparison of IDS and experimental profiles at $x = 5.2208H_{step}$.

The u-velocity profile obtained by the IDS on Figure 4.15 indicates that the flow is still circulating close to the surface. The experimental u-velocity profile, on the other hand, does not indicate the presence of flow circulation. The IDS and experimental data thus show that they have different prediction of the flow reattachment location. The experimental results point to a shorter recirculation region. From Figure 4.14, the u-velocity gradient in the y-direction begins

around $y \geq 1.0\ H_{step}$, for the IDS results. The u-velocity gradient begins later, around $y \leq 1.0\ H_{step}$, for the experimental results. This indicates that the recirculation region is smaller for the experimental data compared to the IDS data. The early start of the u-velocity gradient also indicates that the shearing layer is higher for the IDS data.

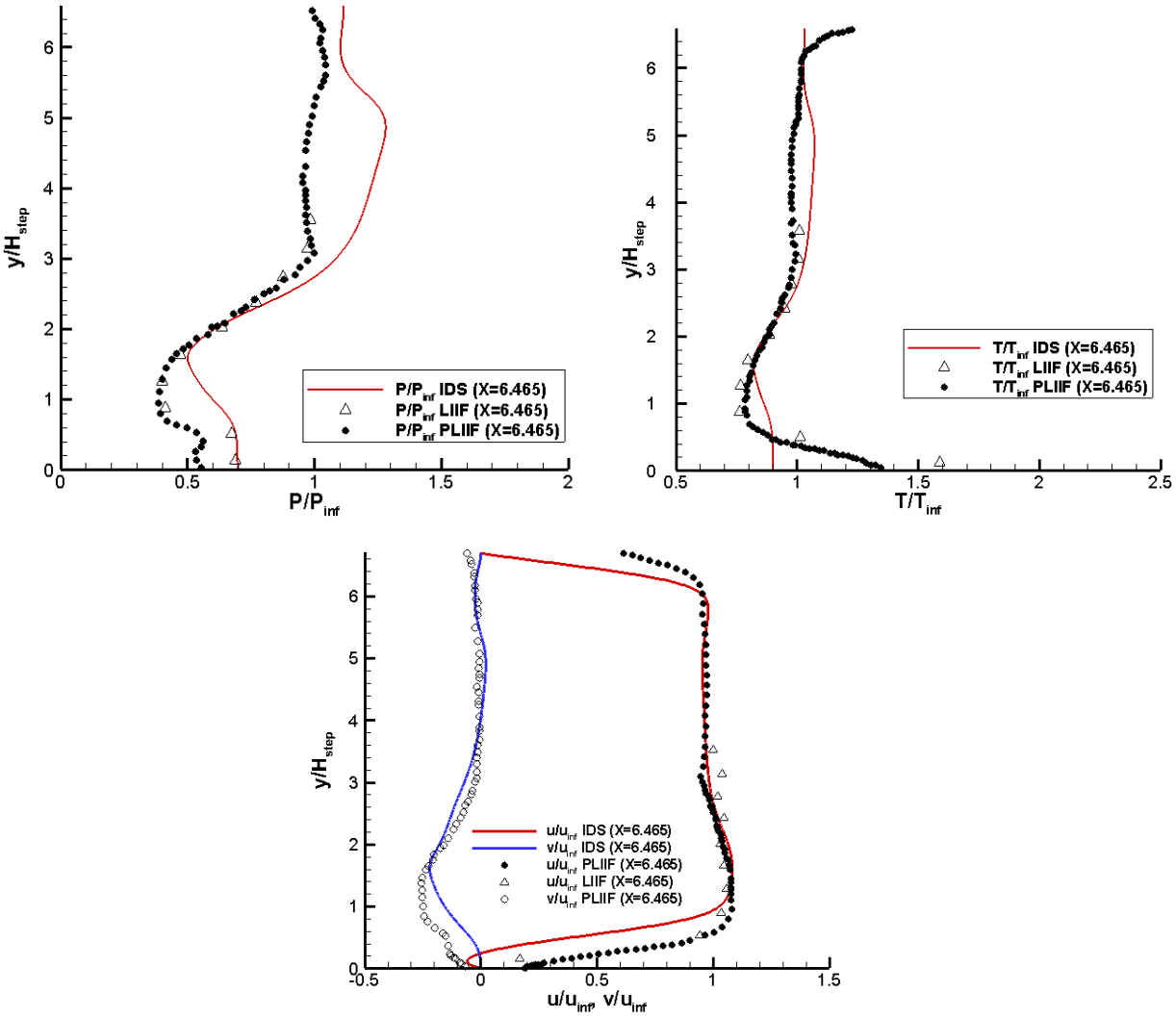

Figure 4.15. Comparison of IDS and experimental profiles at $x = 6.465 H_{step}$.

In Figure 4.16, the flow is downstream of the recirculation region. The profiles therefore will be different from the profiles of Figure 4.14-15. At $x = 10.155\ H_{step}$, the profile display

data that pass through a portion of the expansion fan and the reattachment shock. While tracking pressure from the top surface to the bottom surface, the pressure drops due to the expansion fan and then the pressure increases due to the reattachment shock. This trend can be observed in Figure 4.16. The numerical pressure profile and experimental profile seem to have very good similarity in profile shape; however, the numerical profile seems to be shifted to the right.

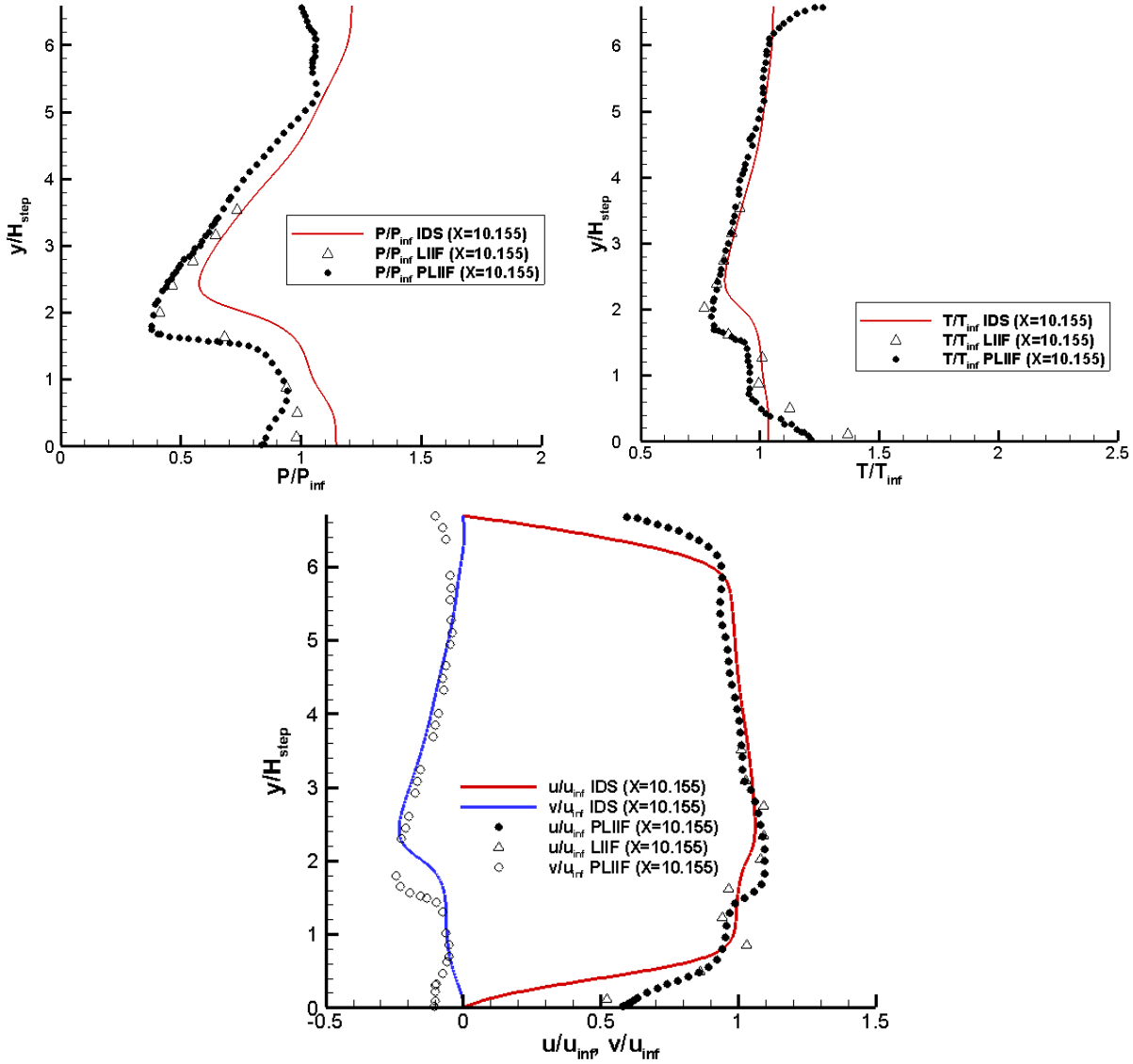

Figure 4.16. Comparison of IDS and experimental profiles at $x = 10.155H_{step}$.

The temperature profile in Figure 4.16 behaves as the pressure profile. That is to say, the temperature gradually drops and then it increases rapidly due to reattachment shock. Inside the

domain, the numerical and experimental temperature profile appear very similar. Towards the surfaces, the temperature profiles are less similar.

The velocity profiles match the experimental data inside the domain. The expansion fan alters the v-velocity to negative values while the u-velocity is increased slightly. The reattachment shock corrects the flow so that it is parallel to the walls. This means that after the shock, the v-velocity is supposed to be zero for the inviscid flow. From the v-velocity profile, these trends are captured well; however, the zero v-velocity after the reattachment shock is not exactly captured. That could be attributed to the fact that the flow is not inviscid. The u-velocity profile appears to look as expected. Close to the walls the experimental and numerical data seem to diverge from each other. The experimental data close to the surface are unable to record the no-slip condition. This inhibits the validation of the boundary condition used by the scheme.

The validation of the scheme is positive for the case of the rearward facing step. Generally, the IDS was able to qualitative and quantitatively capture the flow field physics. The discrepancies that were shown are attributed to the use of wrong boundary conditions. Failure to use boundary conditions that represents the experimental boundary conditions resulted in the appearance of leading edge shocks. Furthermore, disagreements appear to increase as one gets closer to the boundaries. The experimental measurements had issues with recording the correct values close to the surface. Thus experimental issues also contribute to the disagreements that are present.

4.2 Supersonic Flow over Cavity

The second problem that is tackled in the thesis is the supersonic flow over a cavity. This problem has been studied for many years and over a wide range of speeds. The supersonic cavity problem can be applied for aircraft weapons bays, landing gear wells, or flame holders for

scramjets [31]. The supersonic cavity flow has been studied via experiment by many researcher including: S. J. Beresh et al. [31], M. R. Gruber et al. [22], R. Murray and G. Elliott [32], A. Morgenstern and N. Chokani [33]. Other researchers have studied the cavity problem via CFD studies. These researchers include: S. Soltani and R. Hillier [34], J. C. Adams [35], and R. Hillier et al. [36]. These research efforts have contributed to the understanding of the phenomena that are associated with supersonic cavity flows. Figure 4.17 displays the physical characteristics that are expected to be observed for a cavity flow problem. Generally, there are three distinct regions in a cavity flow problem: external flow field, the shear layer, and the recirculation region. The external flow field is the regions outside of the cavity. The shear layer is the layer over the cavity that separates the external flow from the flow inside the cavity. The region inside the cavity is marked by its recirculation flow. Lastly, expansion and compression waves are expected to be observed at the upstream edge and downstream edge of the cavity, respectively.

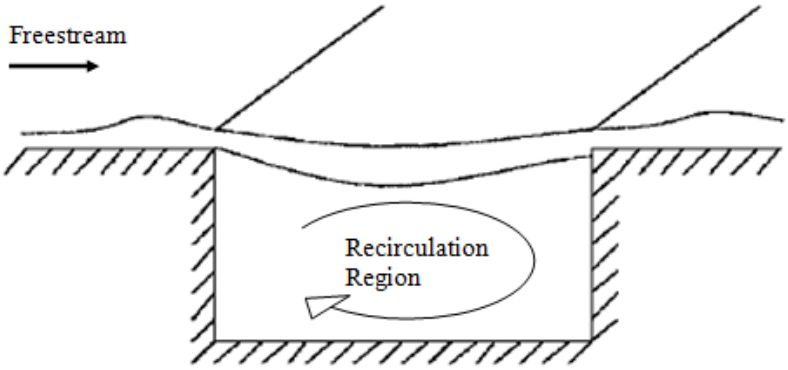

Figure 4.17. Sketch of supersonic flow over cavity problem [22].

4.2.1 Cavity problem setup. For validation, an attempt was made to replicate a supersonic cavity flow experiment that was conducted by M. R. Gruber et al [22]. In the experiment, the cavity that was used had a depth of 8.89 mm with a length to depth ratio of 5.

Figure 4.18 displays the computational geometry that was used in the CFD setup. Table 4.3 displays the flow conditions and properties that were used in the IDS code.

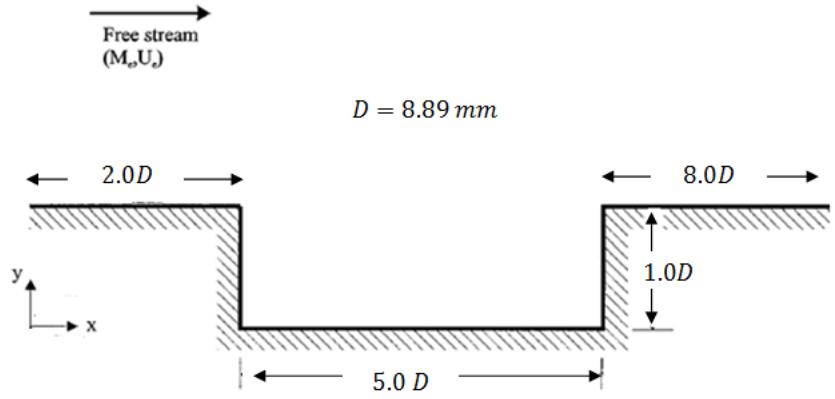

Figure 4.18 Computational cavity [22].

Table 4.3

Supersonic Flow over Cavity Parameters

Parameter	Freestream Condition
Mach at Freestream	3.0
Pressure at Freestream	1.87 KPa
Temperature at Freestream	107.13K
Dynamic viscosity at Freestream	$1.846 \times 10^{-5} - 005\ \frac{J}{m \cdot s}$
Gas constant	$287.0\ \frac{J}{Kg \cdot K}$
Ratio of specific heats	1.4

4.2.2 Cavity problem boundary and initial conditions. The computational domain for the cavity flow problem has a “T” shape. An illustration of the computational domain with color coded boundaries is shown in Figure 4.19. The inlet boundary condition is marked by the red

color. The inlet conditions are calculated based on the inlet information on Table 4.3. The surface is set to a no slip boundary conditions, which is marked by the color blue on Figure 4.19. To increase the resolution and the grid density inside the cavity, only a portion of the vertical space was simulated. As a result, the top surface of the test section was not captured in the domain. The new top boundary condition was set to an outflow boundary condition. The outflow boundary condition is an extrapolation based on the nodes inside the domain, which is color coded green in Figure 4.19. The outflow boundary condition is the same as the one described for the RFS problem. The right boundary is also set to be an outflow boundary condition. For more details, all of the boundary conditions are explained in the RFS problem. Lastly for the initial condition, all of the inner nodes are set to the inlet conditions.

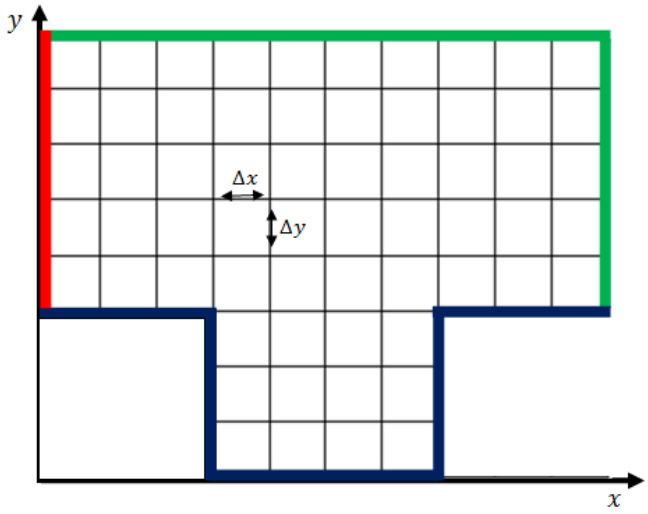

Figure 4.19. Computational domain and boundaries.

4.2.3 Cavity problem results. To solve the cavity flow problem, the boundary conditions, domain, and initial condition were used as inputs for the IDS code. Additionally, the code used a mesh system consisting of 1001 by 1001 grid points. This decision was based on the grid convergence study that was conducted in the RFS investigation. The scheme marched the

initial conditions forward until the steady state criterion was reached. Like in the RFS problem, the convergence criterion was set to a residual of 1.0×10^{-5} or less.

The result that will be presented hereafter ran for 127,876 iterations and reached a final residual of 3.624×10^{-7}. Figure 4.20 displays the solution convergence study. In the figure, it can be observed that the error oscillated for a while before it started decreasing steadily. This could be an indication that the time steps were too large at the beginning.

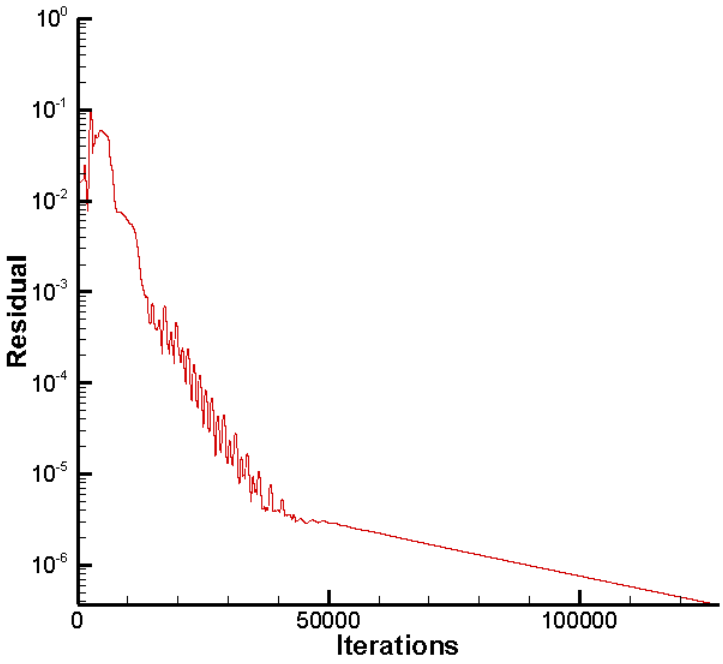

Figure 4.20. Solution convergence study.

Figure 4.21 displays the pressure and temperature contour plots for the flow. For comparison purposes, a shadowgraph and a Schlieren image is displayed on Figure 4.21 as well. In all of the images, the flow is moving from left to right. From the pressure and temperature contour plot there appears a compression wave at the leading edge and a recompression wave at the trailing edge of the cavity. These same features are captured by the experimental flow visualization images, Figure 4.21-C.

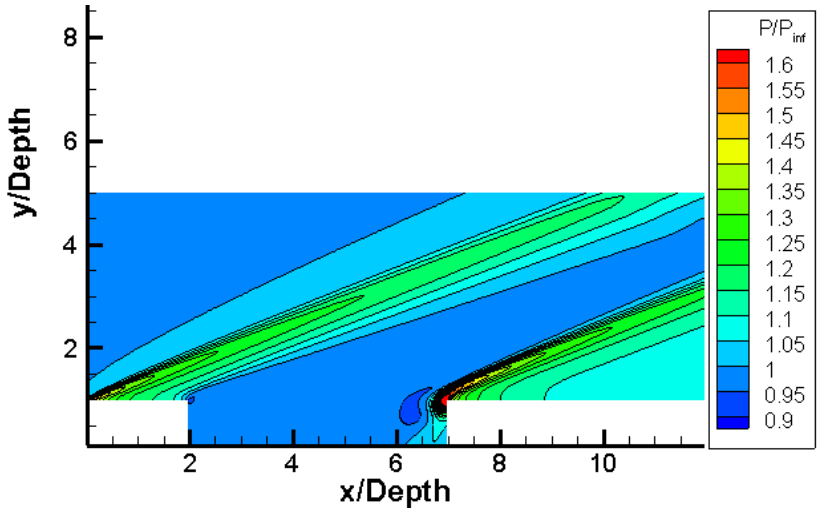

A) Pressure Contour Plot

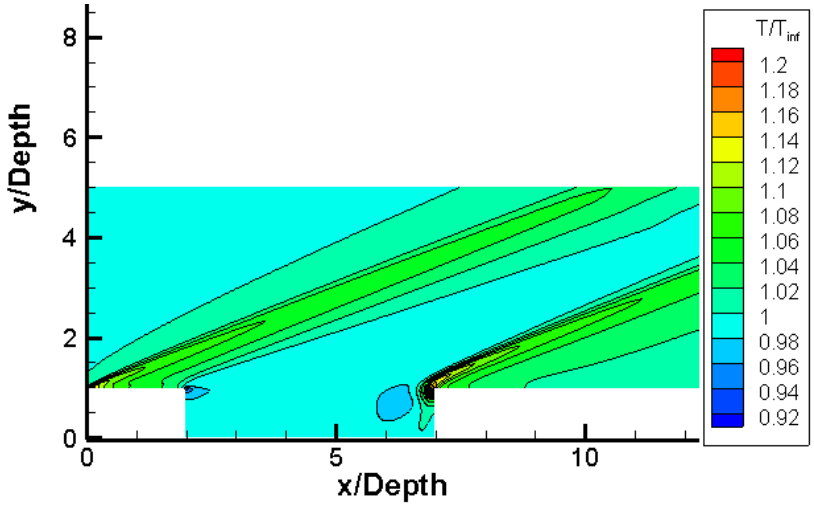

B) Temperature Contour Plot

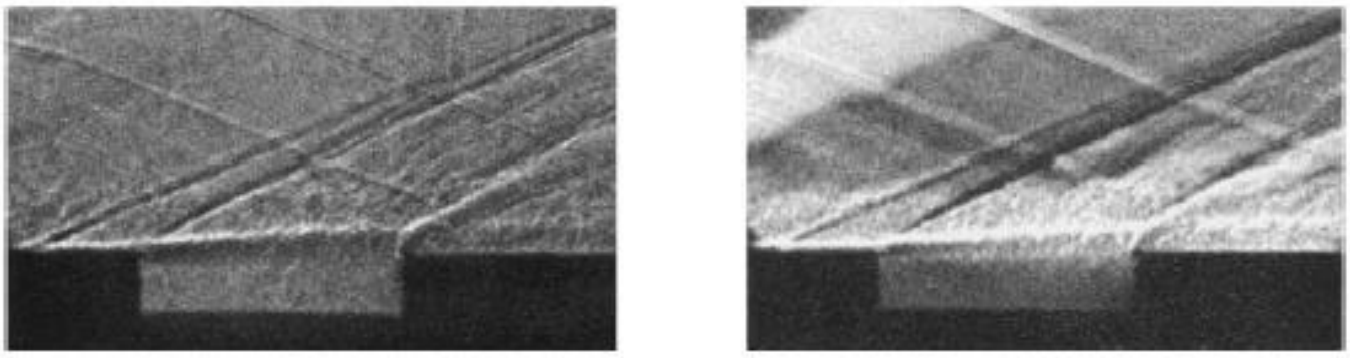

C) Shadowgraph (Left) and Schlieren (right) photographs of Cavity flow fields

Figure 4.21. Contour plots from IDS (A,B) and experimental flow visualization images(C) [22].

Looking at the pressure and temperature contour plot of Figure 4.21, it is clear that at the front corner of the cavity there appears to be an expansion wave, which is distinguished by the decrease in pressure. The expansion wave appears to be very weak. The expansion waves appear in the shadowgraph and schelieren photographs as well. The IDS results captured the same features as the experimental data. Besides the compressive waves and expansion wave, the pressure and temperature in the flow field appears uniform outside the cavity. Inside the cavity the pressure and temperature appear to be relatively uniform as well; although, there are certain regions of high pressure and temperature. These areas are in the aft wall of the cavity.

In Figure 4.22, Mach number contour plot (image A) and velocity contour plots (image B and C) are displayed. In the velocity plots, velocity vectors are superimposed on the contour plots. The boundary layer can be seen in the mach contour plot both upstream and downstream of the cavity. The shear layer detaches from the surface at the leading corner of the cavity and reattaches at the trailing corner of the cavity. The shear layer, seen in the mach contour plots, can be faintly observed in the shadowgraph and schlieren photos (see Figure 4.21 C).In the velocity contour plots (Figure 4.22 B and C), the views have been magnified to focus on the cavity region. The velocity vectors help to identify the shearing region over the cavity, which is identified by the decrease in the velocity vector lengths. Notice that the speed of the flow inside the cavity is very slow relative to the speed outside of the cavity. This trait illustrates why a cavity is a plausible configuration for a supersonic combustor flame holder.

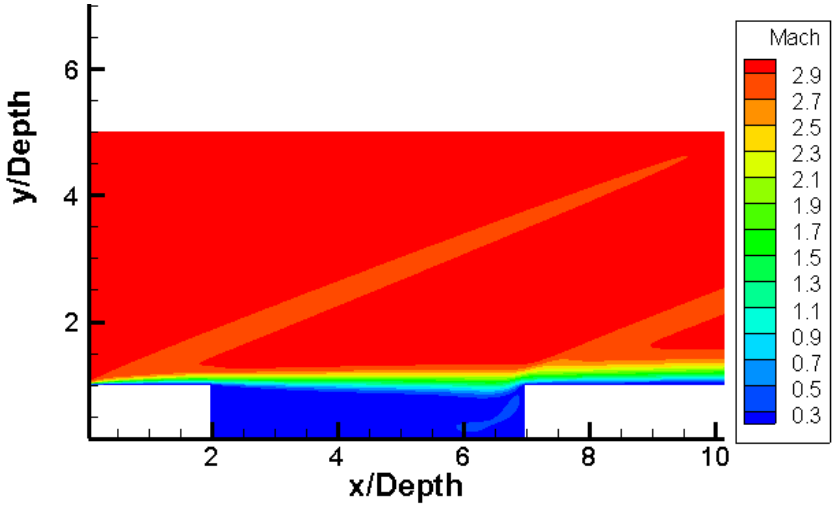

A) Mach Contour

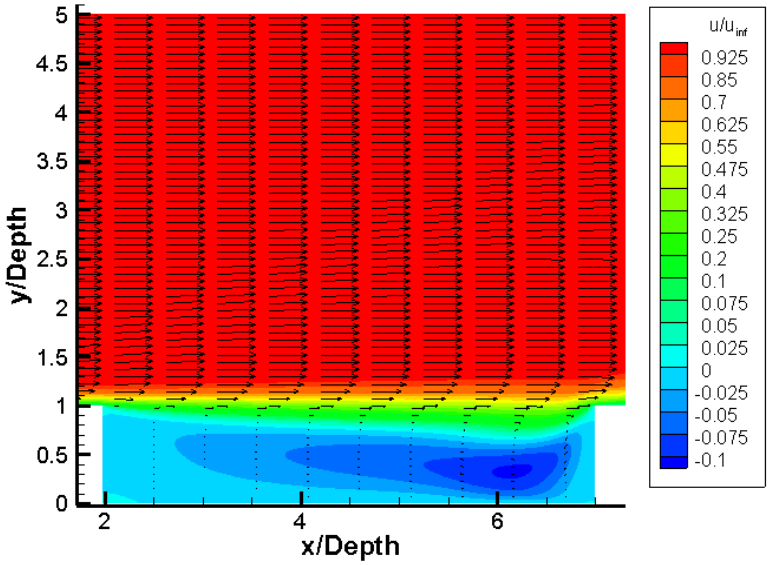

B) U-Velocity Contour

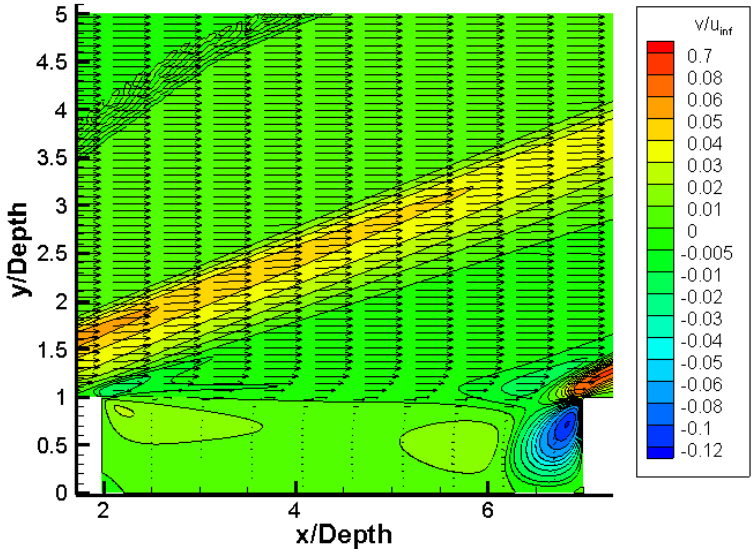

C) V-Velocity Contour

Figure 4.22. Mach number (A) and velocity (B,C) contour plots.

The shear layer is easily identified in the u-velocity contour plot (Figure 4.22 B); however, the shear layer cannot be seen in the v-velocity contour plot (Figure 4.22 C). The v-velocity contour plot gives a forecast of the complex interaction that occurs at the trailing edge of the cavity. In the corner the flow seems to be quickly turned up or down depending on the vertical location. The flow stagnation region is located a small distance below the trail edge of the cavity. Above the stagnation region the flow moves upward and below the stagnation region the flow moves downward. If the flow moves down, it is forced to circulate inside the cavity since it will encounter a bottom wall and even counter the fore wall of the cavity. Once the flow has recirculates to the front wall, it is forced to interact with the external flow. This explanation is supported by the regions of high and low v-velocity in the v-velocity contour plot. Additionally, a streamline plots will further confirm this explanations.

Figure 4.23 shows the streamlines superimposed on the u-velocity contour plot (Figure 4.23 A) and the streamlines superimposed on the pressure contour plot (Figure 4.23 B). Figure 4.23 A is calculated by the IDS code. Figure 4.23 B is calculated by VULCAN Navier-Stokes code. The VULCAN code was used by Gruber et al. as a supplement to their experimental result verification process. In both codes, two recirculation regions are captured. One recirculation region is towards the top right corner of the cavity. This recirculation zone is the larger zone of the two recirculation zones and it extends all the way to the leading edge corner. The second recirculation zone is towards the bottom left corner of the cavity. There are some discrepancies between the shape, location, and size of the recirculation zones between two codes (IDS and VULCAN). The biggest conflict is the size of the smaller recirculation zone. Unfortunately, no experimental data can indicate which of the two images is more accurate. Nevertheless, the main features inside the cavity are captured by both codes.

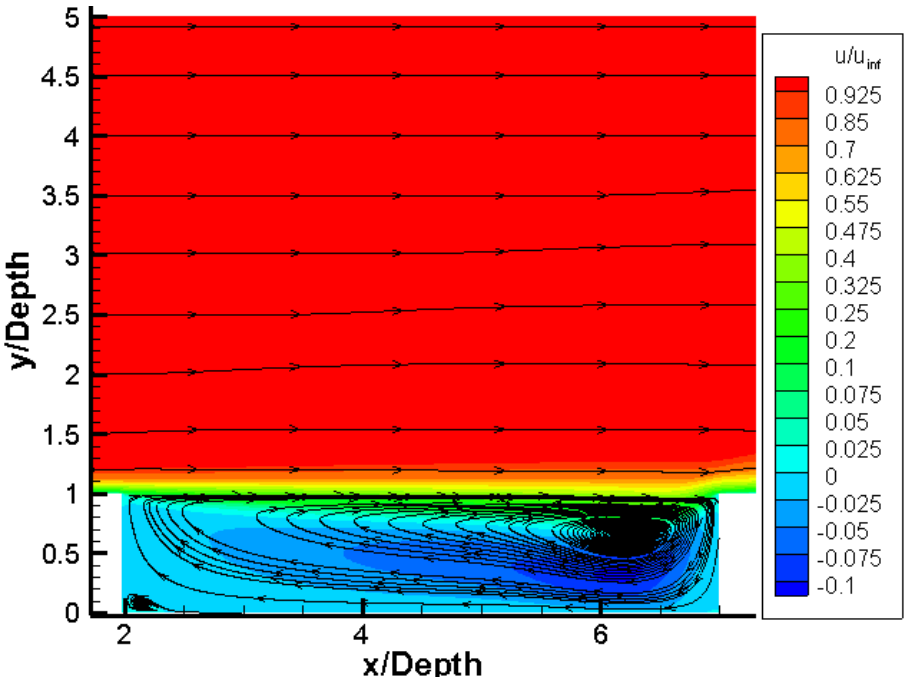

A) IDS Streamlines

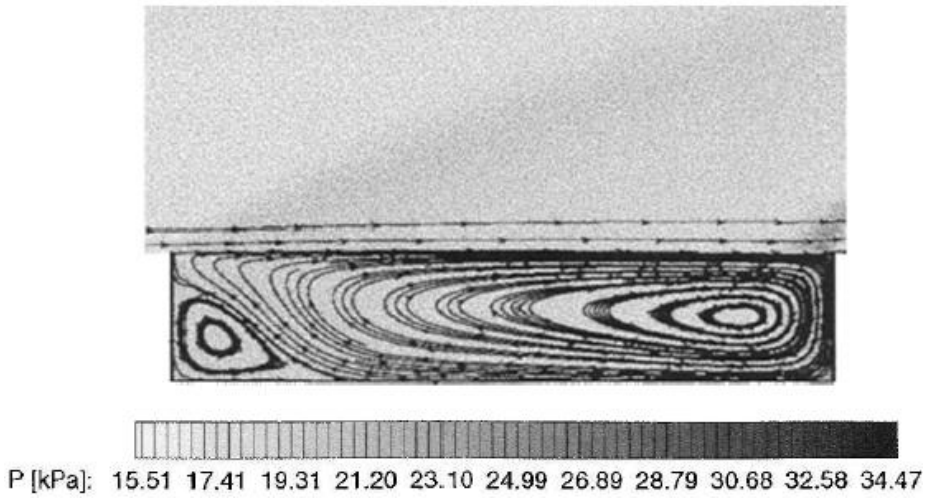

B) VULCAN Streamlines

Figure 4.23. Streamlines comparison for IDS code (A) and VULCAN Navier-Stokes code(B) [22].

Qualitatively, the IDS results are very promising. The next step is to conducted a quantitative comparison between experimental and IDS results. Figure 4.24 shows a pressure plot representing the pressure distribution inside the cavity walls. The experiment data were obtained by pressure measurements. The pressure measurements were conducted using

traditional pressure taps (0.78-mm diameter) to sense the mean wall static pressure along the walls. These measurements were made along the fore, bottom, and aft faces of the cavity. In the pressure plot, the effective distance from 0 to 1 represents the fore cavity wall, from 1 to 6 represents the bottom cavity wall, and from 6 to7 represents the aft cavity wall.

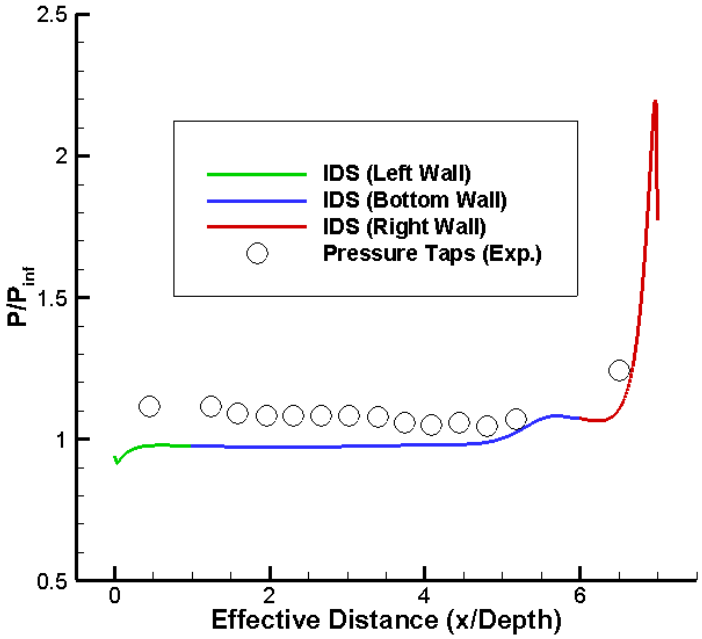

Figure 4.24. Pressure distribution inside the cavity walls [22].

In the beginning of the fore wall, the pressure is slightly low due to the weak expansion, see Figure 4.24. The pressure increases gradually from effective distance of 1 to 6. It can be inferred that the slight pressure rise is due to the accumulating flow at the corner due to the recirculation. Lastly, the pressure increases along the aft cavity until close to the top right corner. After the local pressure ceiling, the pressure drastically decreases. The local pressure maximum corresponds to the stagnation region behind the recompression shock. The drastic pressure drop above the stagnation region is possibly caused by flow spilling over the corner. The flow spillage alleviates the high pressure; thus resulting in a drastic decrease in pressure along the cavity aft wall. The shape of the IDS pressure distribution along the wall resembles the experimental

pressure distribution fairly closely. The offset between the IDS and numerical data can be attributed to experimental data uncertainty or the boundary condition setup.

Inside the domain, the IDS code has been able to present data that qualitatively and quantitatively agrees with the experimental data fairly. Both of problems seem to have the highest discrepancies close to the wall. It is imperative to pick correct boundary condition in order to be able to accurately replicate experiments. Besides the minor discrepancies, the confidence in the Integral-Differential Scheme has been reinforced with this research

CHAPTER 5

Conclusion and Recommendations

This MS thesis documented the technical efforts made to independently validate the Integral-Differential Scheme (IDS). In efforts to push the CFD field forward, this thesis sought to validate the IDS, both quantitatively and qualitatively. Detailed descriptions and analyses of this validation process are provided in Chapter 4, Sections 4.1 and 4.2. As evident by the numerical data files generated by the IDS and the flow field observations made available through the use of TECPLOT 360, it is clear that the IDS has successfully solved the Navier-Stokes equations with a great degree of accuracy. In addition, the IDS generated data supports the fact that the scheme is capable of capturing the flow field physics. It is therefore recommended that great resources be committed to transforming the IDS approach from a code to a CFD tool.

5.1 Conclusion

Based on the results generated from the application of this numerical scheme to a relatively limited number of fluid problems, the IDS demonstrated very promising results. The IDS is designed to solve the integral form of the Navier-Stokes equations. The IDS is based on the finite control volume approach. The scheme was developed with the goal of being simple, robust, and accurate. The scheme is heavily focused on capturing the physics of a given flow field. The new numerical framework can be summarized by the following points:

1. The fluxes through a given cell are calculated based on a linear variation at the cell surfaces.
2. The mean value theorem is used to evaluate the volume and surface integrals.
3. The scheme is an explicit time marching scheme that is based on Taylor's series expansion.

4. The weighted averaging method is set such that each node of interest is based on an averaging of its eight neighboring nodes.

To validate the scheme, two supersonic flow experiments were replicated which a code that was developed for the IDS implementation. The results from the FORTRAN code were analyzed with a post-processing software called TECPLOT 360. The first problem that was tackled was the supersonic flow over a rearward facing step. The IDS was able to capture the flow features of the rearward step problem. These features include: shocks, expansion waves, circulation zone, and the shearing layer. The data obtained were compared to experiment data that were obtained by McDaniel et al. Qualitatively the IDS results and experimental results were very consistent with each other. However, the IDS code captured a leading edge shocks which were not simulated by experiments. The leading edge shocks were induced by the boundary condition setup and not the inaccuracy of the IDS. The interference of the leading edge shock caused the quantitative data to have a discrepancy. These disagreements were most prevalent in the pressure plots. The velocity and temperature plots were not as affected by the presence leading edge shocks.

The second problem that was solved by the IDS was the supersonic flow over cavity. The data obtained were compared to experiment data that were obtained by Gruber et al. The IDS results managed to capture the boundary layers, shearing layer over the cavity, the compression wave, the weak expansion wave, and recirculation region inside the cavity. Qualitatively, the result compared favorably with the experimental shadowgraphs and schlieren photographs. Additionally, a Navier-Stokes code, called VULCAN, calculated the streamlines inside the cavity. The streamlines from both codes (VULCAN and IDS) captured the similar circulation zones. Lastly, the pressure inside the cavity wall was compared with experimental data. The

comparison showed positive trends. Overall, the IDS was able to calculate the flow field accurately given the boundary conditions. Additionally, the results show that choosing correct boundary conditions is vital for CFD validation.

5.2 Future Research Recommendation

The performance of the IDS code in capturing the flow field physics of the two supersonic flow problems of interest to this thesis is extremely encouraging. These outcomes serve to increase the confidence level in the use of the IDS as a tool for fluid dynamics exploration. Of greater importance, these outcomes support the fact that additional investments in resources and time are warranted to further the development of the IDS code into a CFD tool. Improvements in the scheme can be grouped into two areas: scheme improvements and code improvements.

For the case of scheme improvements, the following points are recommended:

- Further validation studies with more complex boundary conditions
- Conduct boundary implementation study
- Improve boundary condition scheme such that curved boundaries can be simulated

For the case of code improvements, the following points are recommended:

- Transform the IDS code using Object Oriented Programming (OOP) techniques.
- Implement the most recent developments in FORTRAN based-compiler that takes advantage of all computational resources. This will allow the executable to run on all of the platforms available for a given workstation.
- Update the IDS code from a serial algorithm to a parallel algorithm.

References

[1] Chakravarthy, S., Goldberg, U., Batten, P., Palaniswamy, S., & Peroomian, O. (2001). Some recent progress in practical computational fluid dynamics. doi: 10.2514/6.2001-136

[2] Oberkampf, William L., & Smith, Barton. (2014). Assessment Criteria for Computational Fluid Dynamics Validation Benchmark Experiments. doi: 10.2514/6.2014-0205

[3] Ijaz, Muhammad. (2010). *Computational Fluid Dynamics: A High-Order Temporal Discretization Method*

[4] M. Behbahani, M. Hormes, U. Steinseifer, D. Arora, O. Coronado, and M. Pasquali. (2009). A Review of Computational Fluid Dynamics

Analysis of Blood Pumps. *European Journal of Applied Mathematics*

[5] Ebrahimi, Houshang. (2004). An Overview of Computational Fluid Dynamics for Application to Advanced Propulsion Systems. doi: 10.2514/6.2004-2370

[6] Elamin, Gafar A. (2008). *The Integral-Differential Scheme (IDS): A New CFD Solver For The System of The Navier-Stokes Equations With Application.* (DOCTOR OF PHILOSOPHY), North Carolina A&T State University.

[7] J. Anderson, G. Degrez, Degroote, E. Dick, R. Grundmann, j. Vierendeels. (2009). *Computational Fluid Dynamics- An Introduction* (3 ed.).

[8] Malalasekera, H. K. Versteeg and W. (2007). *An Introduction to Computational Fluid Dynamics: The Finite Voume Method* (Second Edition ed.).

[9] Brown, Jovan C. (2011). *Validation of the Integral-Differential Scheme as a Navier-Stokes solver via simulation of 2-D Experimental Fluid Studies*

(Master of Science), North Carolina A&T State University.

[10] Frederick Ferguson, Mookesh Dhanasar , Jovan Brown and Isaiah Blankson. (2012). *A Finite Volume Model For Simulating the Unsteady Navier-Stokes Equations Under Space Time Conservations*.

[11] Shang, J. S. (2004). Three decades of accomplishments in computational fluid dynamics. *Progress in Aerospace Sciences, 40*(3), 173-197. doi: 10.1016/j.paerosci.2004.04.001

[12] Harlow, Francis H. (2004). Fluid dynamics in Group T-3 Los Alamos National Laboratory. *Journal of Computational Physics, 195*(2), 414-433. doi: 10.1016/j.jcp.2003.09.031

[13] J. Anderson, E. Dick, G. Degrez, R. Grundmann, J. Degroote, J. Vierendeels. (2009). *Computational Fluid Dynamics: An Introduction* (3rd ed.).

[14] Johnson, Norman L. (2006, 2006). Computational Fluid Dynamics Group: The Legacy of Group T-3. 01-11-2014, from https://www.lanl.gov/orgs/t/t3/history.shtml#intro

[15] Leer, Bram VAn. (2006). Upwind and High-Resolution Methods for Compressible Flow: From Donor Cell to Residual-Distribution Schemes. *Communications in Computational Physics*.

[16] Anderson, John D. (1995). Computational Fluid dynamics : the Basics with Applications.

[17] Chung, T. J. (2002). *Computational Fluid Dynamics*.

[18] Elamin, Gafar A. (2004). *A CFD Scheme Based on a New and Innovative Method of Consistence Averages.* (MASTER OF SCIENCE), North Carolina A&T State University.

[19] Bertin, john J. (2002). *Aerodynamics for Engineers* (4th ed.). KUpper Saddle River, NJ: prentice-Hall, Inc.

[20] Frank P. Incropera, David P. Dewit, Theodore L. Bergman, and Adrienne S. Lavine. (2007). *Fundamentals of Heat and Mass Transfer*.

[21] McDaniel, James, Fletcher, Douglas, Hartfield, R. O. Y., & Hollo, Steven. (1991). Staged Transverse injection into Mach 2 flow behind a rearward-facing step - A 3-D, compressible flow test case for hypersonic combustor CFD validation. doi: 10.2514/6.1991-5071

[22] Gruber, M. R., Baurle, R. A., Mathur, T., & Hsu, K. Y. (2001). Fundamental Studies of Cavity-Based Flameholder Concepts for Supersonic Combustors. *Journal of Propulsion and Power, 17*(1), 146-153. doi: 10.2514/2.5720

[23] Chen, Zhi, Yi, ShiHe, He, Lin, Tian, LiFeng, & Zhu, YangZhu. (2012). An experimental study on fine structures of supersonic laminar/turbulent flow over a backward-facing step based on NPLS. *Chinese Science Bulletin, 57*(6), 584-590. doi: 10.1007/s11434-011-4888-y

[24] Leonard, Rachel and Chokani, Ndaona. (1993). Laser holographic interferometric measurements of the flow behind a rearward facing step. doi: 10.2514/6.1993-3515

[25] Velikorodny, Alexey, Duck, Graham, & Oshkai, Peter. (2010). Experimental investigation of flow over a backward-facing step in proximity to a flexible wall. *Experiments in Fluids, 49*(1), 167-181. doi: 10.1007/s00348-010-0822-3

[26] D. R. Eklund, D. G. Fletcher, R.J. Hartfield JR. , G. B. Northam, and C. L. Dancey. (1995). A Comparative Computational/Experimental Investigation of Mach 2 Flow Over a Rearward-Facing Step. *Computers & Fluids*

[27] Liu, Haixu, Wang, Bing, Guo, Yincheng, Zhang, Huiqiang, & Lin, Wenyi. (2013). Effects of Inflow Mach Number and Step Height on Supersonic Flows over a Backward-Facing Step. *Advances in Mechanical Engineering, 2013*, 1-11. doi: 10.1155/2013/147916

[28] Karimi, Abdullah, Wijeyakulasuriya, Sameera, & Nalim, Mohamed. (2012). Numerical Study of Supersonic Flow over Backward-Facing Step for Scramjet Application. doi: 10.2514/6.2012-4001

[29] Yang, A., Hsieh, W., & Kuo, K. (1991). Theoretical study of supersonic flow separation over a rearward facing step. doi: 10.2514/6.1991-2161

[30] Loth, Eric, Kailasanath, K., & Lohner, Rainald. (1990). Supersonic flow over an axisymmetric backward-facing step. doi: 10.2514/6.1990-1580

[31] Beresh, Steven, Wagner, Justin, & Pruett, Brian. (2012). Particle Image Velocimetry of a Three-Dimensional Supersonic Cavity Flow. doi: 10.2514/6.2012-30

[32] Murray, Robert C., & Elliott, Gregory S. (2001). Characteristics of the Compressible Shear Layer over a Cavity. *AIAA Journal, 39*(5), 846-856. doi: 10.2514/2.1388

[33] Morgenstern, Jr Alagacyr, & Chokani, Ndaona. (1993). Hypersonic flow past open cavities. doi: 10.2514/6.1993-2969

[34] Soltani, Saeed, & Hillier, Richard. (1994). An experimental and computational study of hypersonic cavity flows. doi: 10.2514/6.1994-766

[35] Adams, Jr J. (1974). Numerical calculation of hypersonic laminar cavity flows. doi: 10.2514/6.1974-707

[36] Hillier, R., Boyce, R. R., Creighton, S. A., Fiala, A., Jackson, A. P., Mallinson, S. G., . . . Williams, S. (2003). Development of some hypersonic benchmark flows using CFD and experiment. *Shock Waves, 12*(5), 375-384. doi: 10.1007/s00193-003-0179-0